ACS APPLIED MATERIALS & INTERFACES

www.acsami.org

Research Article

Computational Prediction of Superlubric Layered Heterojunctions

Enlai Gao,[#] Bozhao Wu,[#] Yelingyi Wang, Xiangzheng Jia, Wengen Ouyang, and Ze Liu*

Cite This: https://doi.org/10.1021/acsami.1c04870

Read Online

ACCESS | Metrics & More | Article Recommendations | Supporting Information

ABSTRACT: Structural superlubricity has attracted increasing interest in modern tribology. However, experimental identification of superlubric interfaces among the vast number of heterojunctions is a trial-and-error and time-consuming approach. In this work, based on the requirements on the in-plane stiffnesses of layered materials and the interfacial interactions at the sliding incommensurate interfaces of heterojunctions for structural superlubricity, we propose criteria for predicting structural superlubricity between heterojunctions. Based on these criteria, we identify 61 heterojunctions with potential superlubricity features from 208 candidates by screening the data of first-principles calculations. This work provides a universal route for accelerating the discovery of new superlubric heterojunctions.

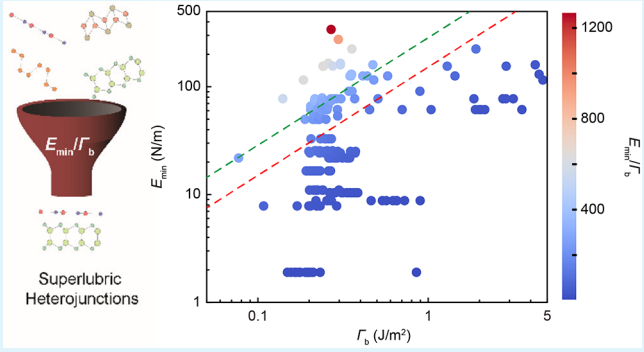

KEYWORDS: *computational prediction, 2D heterojunction, structural superlubricity, friction, first-principles calculations*

INTRODUCTION

Structural superlubricity, or ultralow friction and wear between incommensurate contacting surfaces, is a fascinating phenomenon in the modern tribology that paves a new way toward lubrication.[1−5] An early experimental indication of structural superlubricity was reported for homogeneous MoS_2 interfaces in 1993,[3] and then highly anisotropic friction was observed whereby MoO_3 nanocrystals moved along specific directions on the MoS_2 surface.[6] Clear experimental evidence of structural superlubricity on the nanoscale was demonstrated by Dienwiebel et al.,[5] which showed that the ultralow friction of graphite originates from the incommensurate contact between rotated graphite layers. Afterward, Hod[7] defined a registry index that quantifies the registry mismatch in layered materials and developed a direct relation between interlayer commensurability and ultralow friction in layered materials. Recently, experimental investigations of structural superlubricity were extended to the microscopic scale[8−12] and centimeter-long carbon nanotubes.[13] These remarkable achievements shed light on significantly reducing friction and wear in advanced materials and devices.

However, a major challenge still remains, that is, the observed strong anisotropic friction at the interfaces with respect to their relative orientation, which will disable the structural superlubricity because the incommensurate configuration with ultralow friction prefers to rotate toward the commensurate configuration and thus falls into a high friction state during the sliding.[14] In-plane softness has been predicted to increase the friction in incommensurate contacts because locally commensurate regions can form at the contacting interface,[15−17] and the effect of the in-plane stiffness on structural superlubricity has been examined.[18−20] Fortunately, this issue can promisingly be addressed by assembling sliding layered materials to form heterojunctions[21−23] or by applying strains to the homogeneous interfaces.[24,25] The intrinsic lattice mismatch of the heterojunction surfaces leads to the orientation-independent incommensurate contacts that inhibit the anisotropic friction.[22] For example, Song et al.[23] prepared pristine microscale junctions of graphite/hexagonal boron nitride (*h*-BN) and measured their tribological properties. The orientational anisotropy of the friction at the heterojunction is orders of magnitude lower than that at the homogeneous graphitic interface.

Since experimental identification of superlubric structures among the vast material systems is a trial-and-error and time-consuming approach, only very few of material interfaces have been found to exhibit superlubricity, most of which are the interfaces of layered materials. In this work, we first explore the physical mechanism behind the structural superlubricity and then propose criteria for predicting structural superlubricity between heterojunctions. Based on these criteria, superlubric heterojunctions are discovered by screening the data of first-principles calculations.

Received: March 15, 2021
Accepted: June 16, 2021

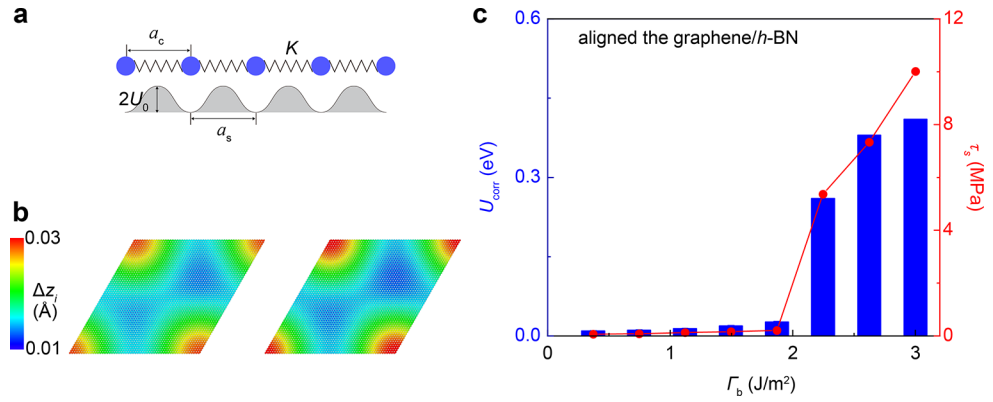

Figure 1. (a) FK model of the 2D heterojunction along the sliding direction, where the springs illustrate the in-plane interatomic interactions, characterized by the stiffness K, and a_c is the lattice parameter of the sliding layer. U_0 and a_s are the amplitude of the interaction potential and the lattice constant of the substrate, respectively. (b) Optimized atomic configurations of the aligned graphene/*h*-BN heterojunction with a low binding energy (left) and a high binding energy (right), in which the carbon atoms are colored by the atomic out-of-plane displacement ($\Delta z = z - z_0$, in which z_0 and z represent the atom position in the z direction before and after optimization). (c) Energy difference ($U_{corr} = 2U_0$) and friction stress (τ_s) during the sliding motion as a function of the binding energy (Γ_b) calculated by using atomistic simulations.

RESULTS AND DISCUSSION

In general, an increase in the interlayer binding energy enhances the interfacial shear strength; for example, the covalent bonds formed at the interfaces of graphene layers and multiwalled carbon nanotubes enhance the energy barrier against interlayer sliding.[26,27] Hence, a decrease in the interlayer interaction of sliding surfaces reduces the interlayer friction. As evidenced, the widely used solid lubrication graphite possesses a low interlayer binding energy (0.14–0.34 J/m^2).[9,28−31] The interlayer binding energy plays a crucial role in sliding systems because it is related to the energy dissipation during the interlayer sliding.[9,32] On the microscale, the in-plane lattices are perturbed by the interlayer binding interaction, which then causes variations in the interatomic configuration when assembling two heterogeneous two-dimensional (2D) materials into a heterojunction. The higher binding energy means the higher atomic interaction that can result in higher lattice deformation. Therefore, it is more likely to induce local commensurate contact (the pinned state) for material pairs with a higher binding energy.[33−35] During the sliding, the pinning and depinning processes take place repeatedly, which causes the lattice vibrations that would be converted to energy dissipation and hence increases the friction. To reveal the mechanism, we first investigate the effect of the binding energy on the amplitude of the interaction potential (U_0) on the basis of the Frenkel–Kontorova (FK) model (Figure 1a).[32] According to the FK model, the criteria of the Aubry transition can be used to identify the state of superlubricity.[36] To describe the Aubry transition, a dimensionless parameter (λ) is introduced as $\lambda = \frac{4\pi^2 U_0}{K a_s^2}$ that represents the ratio of the depth of the potential to the elastic constant, in which K is the stiffness describing the in-plane interatomic interaction and a_s is the lattice constant of the substrate along the sliding direction. There exists a critical value λ_c such that a superlubric state exists for $\lambda < \lambda_c$ and disappears for $\lambda > \lambda_c$. Note that λ_c depends on the incommensurability (a_c/a_s) of the contact surfaces and takes the minimum at an irrational golden mean: $\frac{a_c}{a_s} = \frac{\sqrt{5}-1}{2}$,[32] where a_c is the lattice constant of the sliding layer along the sliding direction.

Similarity obviously exists between the inverse of our below proposed index Γ_b/E_{min} (Γ_b is the binding energy and E_{min} is the smallest in-plane stiffness) and the Aubry transition parameter. To demonstrate this, we first note that in the one-dimensional FK model, K represents the stiffness of the chain describing the interatomic interactions, while for 2D materials, the in-plane stiffness (E) actually reflects interatomic interactions. Therefore, K is expected to be proportional to E ($K \propto E$) in the 2D FK model. Considering the anisotropy of 2D materials, the E_{min} of a layered heterojunction is chosen to characterize its in-plane stiffness. Below, we try to establish the relationship between the lateral corrugation ($U_{corr} = 2U_0$) and the interlayer interaction (binding energy) by using molecular dynamics (MD) simulations (details in Section S1). Taking the graphene/*h*-BN heterojunction as an example (Figure 1b), we observe that both friction stress (τ_s) and U_{corr} linearly increase with increasing Γ_b when Γ_b is small. However, once Γ_b reaches a critical value (~2.2 J/m^2), U_{corr} and τ_s sharply increase, which indicates the Aubry transition.[37] We attribute this transition to the sliding-induced vibration of local interatomic bonds, and a higher Γ_b value can induce larger lateral lattice perturbation and thus lead to significant in-plane deformation (Figure S1c). Therefore, in the regime of $\lambda < \lambda_c$, $\lambda = \frac{4\pi^2 U_0}{K a_s^2}$ is proportional to the ratio Γ_b/E_{min}, which shows the equivalence between the inverse of our index (Γ_b/E_{min}) and the Aubry transition parameter.

To prevent the in-plane deformation of the incommensurate contacts into the local commensurate configuration of high friction by out-of-plane perturbation, high in-plane stiffness of the layered materials for constructing the heterojunction is required. Herein, the out-of-plane perturbation refers to the interlayer interaction, which can induce local lattice deformation and thus local commensurate configuration.[33−35] Based on these insights, we propose the following three criteria for screening potential superlubric heterojunctions:

Criterion 1: Incommensurate contact surfaces, which lead to effective cancellation of the interaction from interfacial sliding atoms.[22,23]

Criterion 2: Low interlayer binding energy of the heterojunction, which reduces the out-of-plane mechanical

https://doi.org/10.1021/acsami.1c04870
ACS Appl. Mater. Interfaces XXXX, XXX, XXX−XXX

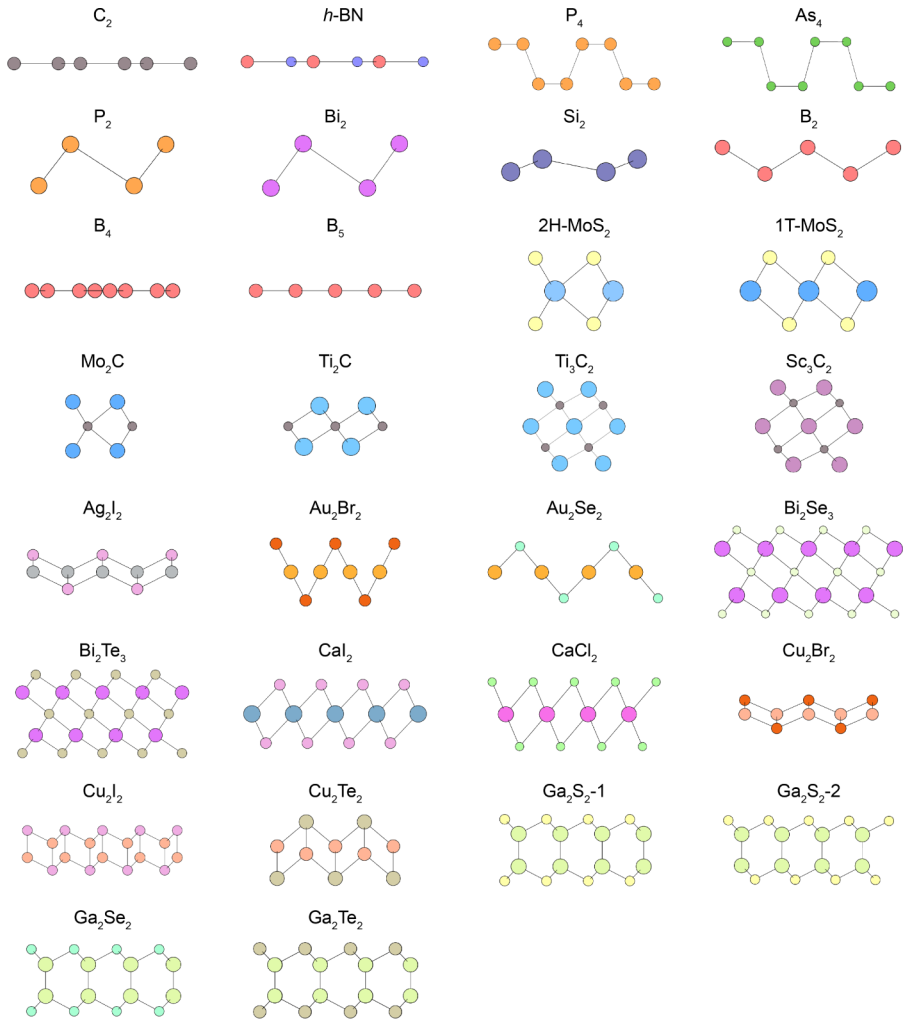

Figure 2. Side views of 30 typical elemental and binary 2D material candidates.

perturbation on the incommensurate contacts during sliding.[33−35]

Criterion 3: High in-plane stiffness of layered heterojunction materials, which minimizes the in-plane deformation of the layered structures and thus maintains the incommensurate contacts during sliding.[15−20]

The search protocol starts with the selection of layered materials from easily exfoliated 2D materials[38] and some other important 2D materials that have been synthesized in experiments for constructing heterojunctions (typical 2D materials candidates are shown in Figure 2). The workflow used to search potential superlubric heterojunctions is illustrated in Figure 3. The 2D materials chosen for constructing heterojunctions include some well-known 2D materials, such as graphene (C_2), silicene (Si_2), *h*-BN, phosphorene (P_4), blue phosphorene (P_2), puckered arsenene (As_4), molybdenum disulfide (1T- and 2H-MoS_2), borophene (B_2, B_4, and B_5), and MXenes (Ti_3C_2, Ti_2C, Sc_3C, and Mo_2C). Unless otherwise noted, the nomenclature of 2D materials in heterojunctions is based on the atom number in the primitive cell of the 2D materials. For example, graphene and phosphorene monolayers are denoted as C_2 and P_4 since there are two carbon and four phosphorus atoms in their primitive cells, respectively. Furthermore, heterojunctions can be constructed from the chosen 2D materials by using the coincidence site lattice method (Figure S2a).[39] The construction of the heterojunctions is detailed in Section S2. Notably, the structural and geometrical parameters used in MD and first-principles calculations are different. In first-principles calculations, to balance the computational cost and the rationality of heterojunction structures, heterojunctions were constructed based on the rules described in Section S2, while the parameters of graphene/*h*-BN heterojunction in MD simulations were adopted from the literature,[23] considering the difference in static calculations and dynamic simulations for first-principles calculations and MD simulations, respectively. As a result, 208 2D heterojunctions were constructed, as summarized in Table S2.

In the first-principles calculations, the DFT-D3 method of Grimme[40] was used to correct the van der Waals (vdW) interactions in the heterojunctions (unless otherwise noted). To validate this method, other common vdW dispersion correction approaches were also used for testing, which agree with the DFT-D3 method (Figure S2b). For example, the binding energies of the C_2/*h*-BN based on DFT-D3, optB86b-vdW, vdW-DF2, and DFT-dDsc are 25, 30, 22, and 27 meV/atom (1 meV/atom = 0.0119 J/m^2), respectively. All these values are very close to the binding energy of the graphene/*h*-BN heterojunction (27.13 meV/atom) calculated with the HSE + MBD DFT method.[35,41,42] These results indicate the reliability of our calculations for the binding energy. The distributions of the calculated binding energy (Γ_b) of our 208

https://doi.org/10.1021/acsami.1c04870
ACS Appl. Mater. Interfaces XXXX, XXX, XXX−XXX

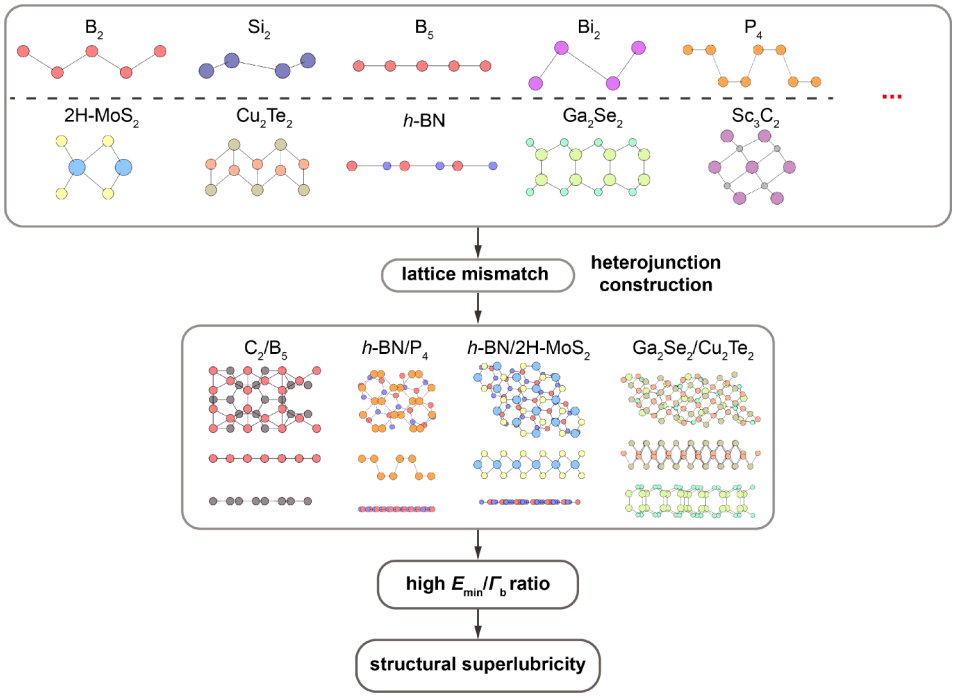

Figure 3. Screening processes of superlubric heterojunctions from 2D material candidates. Typical 2D materials and constructed heterojunctions are illustrated in the inset.

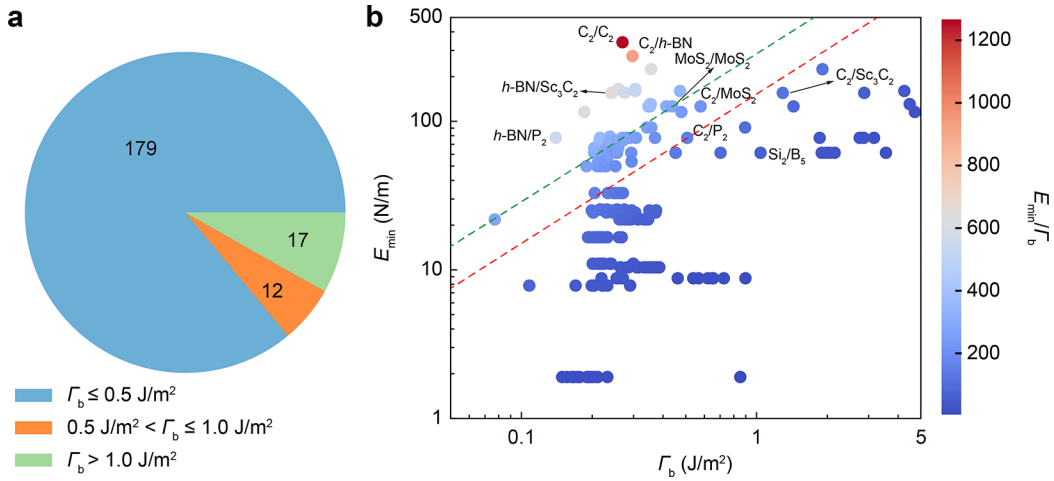

Figure 4. (a) Distributions of the binding energies (Γ_b) of 208 heterojunctions. (b) Map of E_{min} vs Γ_b for 208 heterojunctions and comparison with the C_2/C_2 and MoS_2/MoS_2 interfaces. Based on *criteria 1*−3, the heterojunctions above the green dashed line are predicted to be highly promising superlubric heterojunctions (the experimentally identified superlubric MoS_2/MoS_2 interface lies on the green dashed line), and those between the green and red dashed lines are predicted to be promising superlubric heterojunctions (computationally identified superlubric C_2/P_2 lies on the red dashed line). The data in panel (b) is colored according to the value of ζ.

considered heterojunctions are illustrated in Figure 4a (data in Table S2). The binding energies of these heterojunctions vary from 0.08 J/m^2 (*h*-BN/P_4) to 4.70 J/m^2 (Mo_2C/B_2). The largest binding energy of well-known superlubric structures is of approximately 0.44 J/m^2 (2H-MoS_2/2H-MoS_2), which is below 0.5 J/m^2. Hence, we define the range of $\Gamma_b \leq 0.5$ J/m^2 as the low binding energy range. On the other hand, our first-principles calculations demonstrated that chemical bonds will form at the interfaces when the binding energy is larger than 1.0 J/m^2, e.g., the Si_2B_5 (1.04 J/m^2) and C_2/Sc_3C_2 (1.29 J/m^2) heterojunctions (Figure S3). Notably, the formation of chemical bonds would break down the superlubricity.[43] Hence, we define the range of Γ_b > 1.0 J/m^2 as the high binding energy range. As shown in Figure 4a, we screened 179, 12, and 17 heterojunctions that have the low, moderate, and high binding energies, respectively.

Furthermore, based on *criterion* 3, we assess the in-plane stiffness of the layered materials in the 208 heterojunctions by calculating the minimum in-plane tensile stiffness (E_{min}) of the 2D materials in these heterojunctions. Herein, the in-plane stiffness is $E = Yt$, where Y and t are Young's modulus and the thickness of the 2D materials, respectively. To determine E_{min} of 2D materials, we first obtain the elastic tensors of the 2D materials from first-principles calculations and then E_{min} of each 2D material can be derived from these elastic tensors.[44] Based on the weakest link rule, the smaller E_{min} of the two

https://doi.org/10.1021/acsami.1c04870
ACS Appl. Mater. Interfaces XXXX, XXX, XXX−XXX

materials in a heterojunction was adopted to characterize the in-plane stiffness of this heterojunction, and the data are shown in Table S2.

Based on *criteria* 2−3, E_{min} should be high and Γ_b should be low, which helps maintain the incommensurate configuration (ultralow friction state). The above investigations give a dimensionless index $\zeta = E_{min}/\Gamma_b$, which is used to predict potential superlubric heterojunctions. For the 2D heterojunction with incommensurate contact, when $E_{min}/\Gamma_b < \zeta_c$, where ζ_c is the superlubric threshold, the relative sliding in the heterojunction is thus a high-friction motion. In contrast, if $E_{min}/\Gamma_b > \zeta_c$, there is a continuum set of ground states that can be reached by interlayer sliding through nonrigid displacements of the atoms with ultralow energy cost (smooth motion). By collecting the values of E_{min} and Γ_b from the first-principles calculations, the $E_{min}-\Gamma_b$ map for the 208 heterojunctions (data in Table S2) is shown in Figure 4b, where the junctions distributed in the top-left region are promising superlubric heterojunctions. This region includes some well-known superlubric structures, such as C_2/*h*-BN, C_2/C_2, and MoS_2/MoS_2, which exhibit high ζ values of 927.5, 1266.4, and 287.4, respectively. A highly promising superlubric region was divided above the green dashed line that passes through the experimentally identified superlubric MoS_2/MoS_2 interface with a threshold of ζ_c = 287.4 (Figure 4b). In this region, which contains well-known experimentally identified superlubric structures, there are 25 heterojunctions that are highly promising superlubric structures. In Table 1, we summarize some top-ranked layered junctions based on ζ. Furthermore, we perform friction tests on *h*-BN/Sc_3C_2 and *h*-BN/P_2 heterojunctions with a low Γ_b (0.24 and 0.14 J/m^2, respectively) using first-principles calculations and compare them with bilayer graphene (AB stacking). As shown in Figure 5a, the obtained sliding barrier of the bilayer graphene (using DFT-D3) is smaller than the previous results obtained using the DFT-D method,[45,46] which is ascribed to the equilibrium interlayer distance (d) being calculated by different methods.[46] The observed increase in the sliding barrier with decreasing d (Figure S4a in Section S4) is consistent with the previous reports.[46] Notably, the average friction stress in the *h*-BN/Sc_3C_2 and *h*-BN/P_2 heterojunctions is 4.09 and 9.55 MPa, respectively (in Figure 5b,c). For heterojunctions with moderate binding energies, e.g., the C_2/P_2 heterojunction (ζ = 153.0) with a Γ_b of 0.51 J/m^2, the average friction stress was determined as 1.46 MPa. Among the heterojunctions, the C_2/Sc_3C_2 heterojunction has a ζ value of 120.1 close to that of the C_2/P_2 heterojunction (Figure 4b). The average friction stress of the C_2/Sc_3C_2 heterojunction was determined to be 271.78 MPa (Figure 5e), much larger than that of the C_2/P_2 heterojunction, which indicates a high friction state. Therefore, we can draw the red dashed line passing through the computationally identified potential superlubric C_2/P_2 heterojunction as the edge of the superlubric region with the threshold of ζ_c = 153.0. Based on these physical considerations, 36 heterojunctions located in the region between the green and red dashed lines are predicted to be promising superlubric heterojunctions. Remarkably, direct experimental evidence recently showed the superlubric feature of the C_2/MoS_2 heterojunction[47] with a moderate binding energy of 0.58 J/m^2, which is one of predicted members using our search criteria. Overall, the heterojunctions distributed in the top-left region (Figure 4b) above the red line are promising for exhibiting superlubric features.

Table 1. List of Top-Ranked Layered Junctions with Structural Superlubricity Based on $\zeta = E_{min}/\Gamma_b$, Including Some Experimentally Identified Superlubric Materials Found Based on Our Search Criteria

junctions	E_{min}/Γ_b	remarks
C_2/C_2	1266.4	known
C_2/*h*-BN	927.5	known
h-BN/Sc_3C_2	645.7	
h-BN/B_4	641.0	
h-BN/B_5	638.4	
h-BN/Ti_3C_2	629.3	
C_2/Mo_2C	624.7	
C_2/B_4	566.0	
h-BN/P_2	554.0	
C_2/B_5	541.7	
C_2/B_2	525.2	
MoS_2/MoS_2	287.4	known
C_2/MoS_2	218.1	known

Progress in applications of superlubricity will be accelerated, since our work extends the family of the superlubric heterojunctions. A noticeable feature of predicted superlubric heterojunctions in Table 1 is that there are a variety of materials with fantastic properties, which could facilitate advanced engineering applications of superlubricity. On the one hand, the predicted superlubric heterojunctions contain materials of superconductors (e.g., Mo_2C),[48] conductors (e.g., B_2),[49] semimetals (e.g., C_2),[50] semiconductors (e.g., MoS_2),[51] and insulators (e.g., *h*-BN),[52] the combinations of which will allow us to study, for example, the contribution of electrons and phonons to superlubricity,[53] and to design smart devices with tunable properties.[20] On the other hand, some predicted heterojunctions possess other interesting functionalities. For instance, phosphorene (P_4) exhibits high optical and UV absorption, which is of particular interest for optoelectronic applications;[54] hence, the C_2/P_4 heterojunction can be operated as a promising saturable absorber for ultrafast laser systems with ultrahigh pulse energy and ultranarrow pulse duration.[55] As recently reported that by exploiting superlubric motion, the modulation voltage of graphene optoelectronic devices can be 1−3 orders of magnitude lower than the voltage of traditional electro-optic modulators, while the modulation response is approximately 4 orders of magnitude faster than the speed of traditional mechanical modulation.[56]

In addition, considering that structural superlubricity has been realized/predicted only in several crystalline materials with atomically smooth surfaces (e.g., planar monocrystalline graphene, *h*-BN, and MoS_2 surfaces) at small scales (e.g., 1 nm to 10 μm),[5,8,23,57] we characterize the surface smoothness of 2D materials by measuring the surface area per atom, S_{atom} (nm^2/atom), and the altitude difference, Δh (Å), between the surface and subsurface atoms along the out-of-plane direction (Figure S5a,b in Section S5) for the considered 2D materials (Figure 2). We observe that S_{atom} and Δh show positive correlations in the ranges of S_{atom} = 0.03−0.26 nm^2/atom and Δh = 0−2.45 Å (Figure 5f). The above investigations and the observed Aubry transition (Figure 1c) indicate that a high Γ_b value could cause a large interatomic deformation at the contact surfaces and breaking of smooth surfaces. Additionally, the binding-energy-dependent interatomic deformation is evident from the first-principles calculations, which show

https://doi.org/10.1021/acsami.1c04870
ACS Appl. Mater. Interfaces XXXX, XXX, XXX−XXX

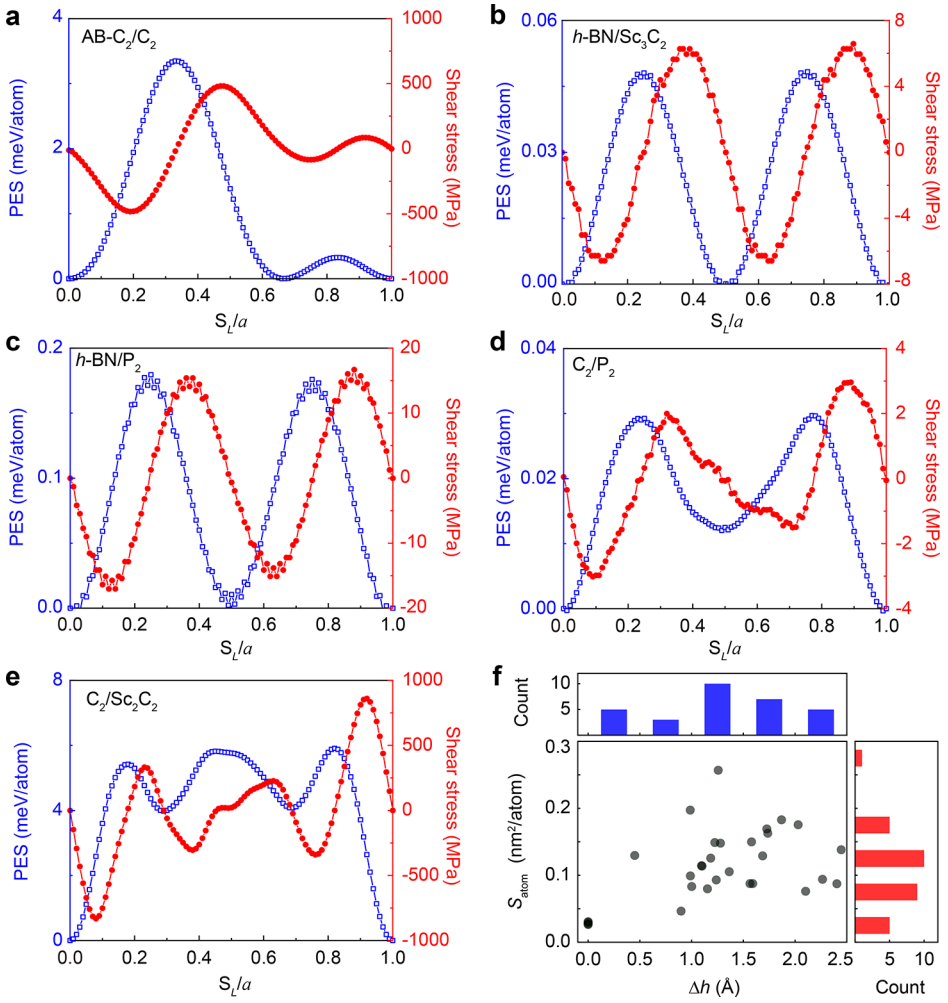

Figure 5. Sliding potential energy surface (PES) (left axis, blue cubes) and the corresponding friction stress (right axis, red points) as a function of the sliding length (S_L) from first-principles calculations for (a) bilayer graphene (AB stacking), (b) *h*-BN/Sc_3C_2, (c) *h*-BN/P_2, (d) C_2/P_2, and (e) C_2/Sc_3C_2 heterojunctions. In panel (a), the top layer slides along the armchair direction, while for the remaining configurations (b–d), the top layer slides along the *x* direction (see Figure S5a,c and Section S5). Here, the sliding PES is shifted relative to the global energy minimum along the sliding path. The calculated Γ_b for the heterojunctions in panels (a), (b), (c), (d) and (e) are 0.27, 0.24, 0.14, 0.51, and 1.29 J/m^2, respectively. (f) Measured area of surface atoms (S_{atom}) and the altitude difference (Δh, see the definition in Figure S5 and Section S5) between atoms for considered 2D materials, and the top and right panels show the histograms for S_{atom} and Δh.

significant interatomic deformations and reduced interlayer distances in the heterojunctions with a high binding energy (Γ_b > 1 J/m^2), for example, Si_2/B_5 (1.04 J/m^2) and C_2/Sc_3C_2 (1.29 J/m^2) heterojunctions (Figure S3). Additionally, the first-principles calculations indicate the disappearance of the superlubric state for the C_2/Sc_3C_2 heterojunction (Figure S3b) with an average friction stress of 271.78 MPa (Figure 5e). Therefore, we further conclude that heterojunctions exhibiting weak interlayer interactions help maintain the atomically smooth interface, which is consistent with the previous work on tin monochalcogenide heterostructures.[58] Notably, the results in Figure S4 and the previous work[45,46] demonstrate that the frictional shear stress depends on the interlayer distance. To further validate this dependence for other material pairs, we take the C_2/P_2 heterojunction as an example to investigate the dependence of frictional shear stress on the layer spacing. These results also indicate that the sliding energy barriers and the frictional shear stresses increase with the decrease of layer spacing (Figure S5d,e).

Finally, the influences of the relative orientation and sliding direction are discussed below. Since a large number of heterojunctions were considered in this work and it would be a huge task to study these influences for each heterojunction, we take the C_2/P_2 heterojunction as a case to probe the influences of the relative orientation and sliding direction on the friction (see details in Section S6). Herein, we explore the C_2/P_2 heterojunctions with four misfit angles (0°, 10.89°, 14.39°, and 19.11°). The atomic configurations and friction traces are shown in Figure S6. It can be found that in the range of 0–19.11°, the average friction stress decreases (9.90–1.46 MPa) with the increase of the misfit angle (Figure S7a). Notably, similar behavior has also been reported in the graphene/*h*-BN heterojunction.[23,33,59] On the other hand, different sliding directions were further explored (see details in Section S6). The maximum sliding energy barrier of 0.0325 meV/atom (Figure S7b) is only slightly larger than that along the *x* direction (0.0297 meV/atom, Figure 5d), indicating that the influence of the sliding direction is quite small.

CONCLUSIONS

In summary, we propose universal criteria for predicting the structural superlubricity of heterojunctions by considering the

https://doi.org/10.1021/acsami.1c04870
ACS Appl. Mater. Interfaces XXXX, XXX, XXX−XXX

requirements on the in-plane stiffness of layered materials and the interlayer interaction at the sliding incommensurate interface of heterojunctions for structural superlubricity. Afterward, we characterize the in-plane stiffness and interfacial binding energies of 208 heterojunctions by using first-principles calculations. Combining the proposed criteria and first-principles calculations, new superlubric heterojunctions and known identified superlubric structures were discovered based on our search criteria, which are well supported by atomistic simulations and existing experiments. The variety of predicted superlubric heterojunctions could facilitate the design and wide application of superlubricity-based devices.

COMPUTATIONAL METHODS

To calculate the fundamental properties of heterojunctions, first-principles calculations based on density functional theory[60,61] were performed by using the Vienna Ab initio Simulation Package (VASP).[62] The projector augmented wave method was used to treat the interactions between electrons and ions.[63] The generalized gradient approximation of the Perdew–Burke–Ernzerhof functional[64] was employed to describe the exchange and correlation interactions among electrons. The default highest value was used for the energy cutoff in all cases (e.g., the cutoff of 400 eV was used for C_2/P_2). To reliably correct vdW dispersion, we first performed tests on the basis of the common vdW dispersion correction approaches of DFT-D3,[40] optB86b-vdW,[65] vdW-DF2,[66] and DFT-dDsC.[67] Unless otherwise noted, the DFT-D3 method of Grimme[40] was used to correct the vdW interactions in heterojunctions. Monkhorst–Pack grid *k*-points[68] with a resolution value between *k*-points in the reciprocal cell of less than 0.25 $Å^{-1}$ were used for Brillouin zone sampling in the 2D heterojunction relaxations and of less than 0.12 $Å^{-1}$ were used for the calculations of in-plane stiffness and friction traces. A vacuum layer of 20 Å was used to isolate neighboring periodic images. For the ion relaxations of all of the structures, the convergence criterion was 0.01 eV/Å for the force on each atom by using the conjugate gradient algorithm. The hybridization of wave functions was not considered here, since it has little effect on the mechanical properties of heterojunctions, including the in-plane stiffness and interlayer interactions.[69,70] The friction tests are performed as follows. Starting from the fully relaxed configurations, the shear deformation is applied by transversely moving one layer with respect to its neighbor, step by step. After the rigid displacement between the two layers, the degrees of freedom of all atoms are fixed for calculating the system energy. Then, a series of sliding potential energies along the sliding path can be obtained. The frictional shear stress is obtained from the energy–displacement curve.

ASSOCIATED CONTENT

Supporting Information

The Supporting Information is available free of charge at https://pubs.acs.org/doi/10.1021/acsami.1c04870.

> Molecular dynamics simulation protocol; rules of constructing heterojunctions and different vdW dispersion corrections for the calculations of interlayer binding energy; effects of high binding energy on the lattice deformation of the heterojunction; effects of interlayer distances on the sliding PES and shear stress; heterojunction configurations used in the friction tests and the calculations of surface smoothness; influences of the relative orientation and sliding direction on the friction; and Table S2 including the detailed parameters and results in our first-principles calculations (PDF)

AUTHOR INFORMATION

Corresponding Author

Ze Liu − *Department of Engineering Mechanics, School of Civil Engineering, Wuhan University, Wuhan, Hubei 430072, China;* orcid.org/0000-0002-9906-5351; Email: ze.liu@whu.edu.cn

Authors

Enlai Gao − *Department of Engineering Mechanics, School of Civil Engineering, Wuhan University, Wuhan, Hubei 430072, China;* orcid.org/0000-0003-1960-0260

Bozhao Wu − *Department of Engineering Mechanics, School of Civil Engineering, Wuhan University, Wuhan, Hubei 430072, China*

Yelingyi Wang − *Department of Engineering Mechanics, School of Civil Engineering, Wuhan University, Wuhan, Hubei 430072, China*

Xiangzheng Jia − *Department of Engineering Mechanics, School of Civil Engineering, Wuhan University, Wuhan, Hubei 430072, China*

Wengen Ouyang − *Department of Engineering Mechanics, School of Civil Engineering, Wuhan University, Wuhan, Hubei 430072, China;* orcid.org/0000-0001-8700-1978

Complete contact information is available at: https://pubs.acs.org/10.1021/acsami.1c04870

Author Contributions

#E.G. and B.W. contributed equally to this work.

Notes

The authors declare no competing financial interest.

ACKNOWLEDGMENTS

This work was supported by the Wuhan Science and Technology Bureau of China through Grant 2019010701011390, and the National Natural Science Foundation of China through Grants 11872284, 11902225, 11890673, and 11890674. The numerical calculations in this work have been performed on a supercomputing system in the Supercomputing Center of Wuhan University.

REFERENCES

(1) Hirano, M.; Shinjo, K. Atomistic Locking and Friction. *Phys. Rev. B* **1990**, *41*, 11837–11851.

(2) Hirano, M.; Shinjo, K. Superlubricity and Frictional Anisotropy. *Wear* **1993**, *168*, 121–125.

(3) Martin, J. M.; Donnet, C.; Le Mogne, T.; Epicier, T. Superlubricity of Molybdenum Disulphide. *Phys. Rev. B* **1993**, *48*, 10583–10586.

(4) Shinjo, K.; Hirano, M. Dynamics of Friction: Superlubric State. *Surf. Sci.* **1993**, *283*, 473–478.

(5) Dienwiebel, M.; Verhoeven, G. S.; Pradeep, N.; Frenken, J. W. M.; Heimberg, J. A.; Zandbergen, H. W. Superlubricity of Graphite. *Phys. Rev. Lett.* **2004**, *92*, No. 126101.

(6) Sheehan, P. E.; Lieber, C. M. Nanotribology and Nanofabrication of MoO_3 Structures by Atomic Force Microscopy. *Science* **1996**, *272*, 1158–1161.

(7) Hod, O.; Commensurability, I. Superlubricity in Rigid Layered Materials. *Phys. Rev. B* **2012**, *86*, No. 075444.

(8) Liu, Z.; Yang, J.; Grey, F.; Liu, J. Z.; Liu, Y.; Wang, Y.; Yang, Y.; Cheng, Y.; Zheng, Q. Observation of Microscale Superlubricity in Graphite. *Phys. Rev. Lett.* **2012**, *108*, No. 205503.

(9) Koren, E.; Lörtscher, E.; Rawlings, C.; Knoll, A. W.; Duerig, U. Adhesion and Friction in Mesoscopic Graphite Contacts. *Science* **2015**, *348*, 679–683.

(10) Vu, C. C.; Zhang, S.; Urbakh, M.; Li, Q.; He, Q. C.; Zheng, Q. Observation of Normal-Force-independent Superlubricity in Mesoscopic Graphite Contacts. *Phys. Rev. B* **2016**, *94*, No. 081405(R).
(11) Sheehan, P. E.; Lieber, C. M. Friction between Van der Waals Solids During Lattice Directed Sliding. *Nano Lett.* **2017**, *17*, 4116−4121.
(12) Liu, S.-W.; Wang, H.-P.; Xu, Q.; Ma, T.-B.; Yu, G.; Zhang, C.; Geng, D.; Yu, Z.; Zhang, S.; Wang, W.; Hu, Y.-Z.; Wang, H.; Luo, J.; Microscale, R. Superlubricity under High Contact Pressure Enabled by Graphene-Coated Microsphere. *Nat. Commun.* **2017**, *8*, No. 14029.
(13) Zhang, R.; Ning, Z.; Zhang, Y.; Zheng, Q.; Chen, Q.; Xie, H.; Zhang, Q.; Qian, W.; Wei, F. Superlubricity in Centimetres-Long Double-walled Carbon Nanotubes under Ambient Conditions. *Nat. Nanotechnol.* **2013**, *8*, 912−916.
(14) Filippov, A. E.; Dienwiebel, M.; Frenken, J. W. M.; Klafter, J.; Urbakh, M. Torque and Twist against Superlubricity. *Phys. Rev. Lett.* **2008**, *100*, No. 046102.
(15) Sorensen, M. R.; Jacobsen, K. W.; Stoltze, P. Simulations of Atomic-scale Sliding Friction. *Phys. Rev. B* **1996**, *53*, No. 2101.
(16) Müser, M. H. Structural Lubricity: Role of Dimension and Symmetry. *Europhys. Lett.* **2004**, *66*, 97−103.
(17) Kim, W. K.; Falk, M. L. Atomic-scale Simulations on the Sliding of Incommensurate Surfaces: The Breakdown of Superlubricity. *Phys. Rev. B* **2009**, *80*, No. 235428.
(18) Ma, M.; Benassi, A.; Vanossi, A.; Urbakh, M. Critical Length Limiting Duperlow Friction. *Phys. Rev. Lett.* **2015**, *114*, No. 055501.
(19) Babagholami, B.; Sadeghi, A.; Etezadifar, M. Partial Commensuration and Amontons Laws of Friction Adapted for Large Atomic Interfaces. *Phys. Rev. B* **2019**, *99*, No. 165412.
(20) Vanossi, A.; Bechinger, C.; Urbakh, M. Structural Lubricity in Soft and Hard Matter Systems. *Nat. Commun.* **2020**, *11*, No. 4657.
(21) Leven, I.; Krepel, D.; Shemesh, O.; Hod, O. Robust Superlubricity in Graphene/*h*-BN Heterojunctions. *J. Phys. Chem. Lett.* **2013**, *4*, 115−120.
(22) Mandelli, D.; Leven, I.; Hod, O.; Urbakh, M. Sliding Friction of Graphene/Hexagonal-Boron Nitride Heterojunctions: A Route to Robust Superlubricity. *Sci. Rep.* **2017**, *7*, No. 10851.
(23) Song, Y.; Mandelli, D.; Hod, O.; Urbakh, M.; Ma, M.; Zheng, Q. Robust Microscale Superlubricity in Graphite/Hexagonal Boron Nitride Layered Heterojunctions. *Nat. Mater.* **2018**, *17*, 894−899.
(24) Wang, K.; Ouyang, W.; Cao, W.; Ma, M.; Zheng, Q. Robust Superlubricity by Strain Engineering. *Nanoscale* **2019**, *11*, 2186−2193.
(25) Androulidakis, C.; Koukaras, E. N.; Paterakis, G.; Trakakis, G.; Galiotis, C. Tunable Macroscale Structural Superlubricity in Two-Layer Graphene via Strain Engineering. *Nat. Commun.* **2020**, *11*, 1−11.
(26) Huang, X.; Yuan, H.; Liang, W.; Zhang, S. Mechanical Properties and Deformation Morphologies of Covalently Bridged Multi-walled Carbon Nanotubes: Multiscale Modeling. *J. Mech. Phys. Solids* **2010**, *58*, 1847−1862.
(27) Telling, R. H.; Ewels, C. P.; El-Barbary, A. A.; Heggie, M. I. Wigner Defects Bridge the Graphite Gap. *Nat. Mater.* **2003**, *2*, 333−337.
(28) Zacharia, R.; Ulbricht, H.; Hertel, T. Interlayer Cohesive Energy of Graphite from Thermal Desorption of Polyaromatic Hydrocarbons. *Phys. Rev. B* **2004**, *69*, No. 155406.
(29) Kolmogorov, A. N.; Crespi, V. H. Registry-dependent Interlayer Potential for Graphitic Systems. *Phys. Rev. B* **2005**, *71*, No. 235415.
(30) Spanu, L.; Sorella, S.; Galli, G. Nature and Strength of Interlayer Binding in Graphite. *Phys. Rev. Lett.* **2009**, *103*, No. 196401.
(31) Liu, Z.; Liu, J. Z.; Cheng, Y.; Li, Z.; Wang, L.; Zheng, Q. Interlayer Binding Energy of Graphite: A Mesoscopic Determination from Deformation. *Phys. Rev. B* **2012**, *85*, No. 205418.
(32) Vanossi, A.; Manini, N.; Urbakh, M.; Zapperi, S.; Tosatti, E. Colloquium: Modeling Friction: From Nanoscale to Mesoscale. *Rev. Mod. Phys.* **2013**, *85*, 529−552.
(33) Van Wijk, M. M.; Schuring, A.; Katsnelson, M. I.; Fasolino, A. Moiré Patterns as a Probe of Interplanar Interactions for Graphene on *h*-BN. *Phys. Rev. Lett.* **2014**, *113*, No. 135504.
(34) Feng, S.; Xu, Z. Pattern Development and Control of Strained Solitons in Graphene Bilayers. *Nano Lett.* **2021**, *21*, 1772−1777.
(35) Ouyang, W.; Mandelli, D.; Urbakh, M.; Hod, O. Nanoserpents: Graphene Nanoribbon Motion on Two-dimensional Hexagonal Materials. *Nano Lett.* **2018**, *18*, 6009−6016.
(36) Peyrard, M.; Aubry, S. Critical Behaviour at the Transition by Breaking of Analyticity in the Discrete Frenkel-Kontorova Model. *J. Phys. C: Solid State Phys.* **1983**, *16*, 1593−1608.
(37) Brazda, T.; Silva, A.; Manini, N.; Vanossi, A.; Guerra, R.; Tosatti, E.; Bechinger, C. Experimental Observation of the Aubry Transition in Two-dimensional Colloidal Monolayers. *Phys. Rev. X* **2018**, *8*, No. 011050.
(38) Mounet, N.; Gibertini, M.; Schwaller, P.; Campi, D.; Merkys, A.; Marrazzo, A.; Sohier, T.; Castelli, I. E.; Cepellotti, A.; Pizzi, G.; Marzari, N. Two-Dimensional Materials from High-throughput Computational Exfoliation of Experimentally Known Compounds. *Nat. Nanotechnol.* **2018**, *13*, 246−252.
(39) Koda, D. S.; Bechstedt, F.; Marques, M.; Teles, L. K. Coincidence Lattices of 2D Crystals: Heterostructure Predictions and Applications. *J. Phys. Chem. C* **2016**, *120*, 10895−10908.
(40) Grimme, S.; Antony, J.; Ehrlich, S.; Krieg, H. A Consistent and Accurate Ab Initio Parametrization of Density Functional Dispersion Correction (DFT-D) for the 94 Elements H-Pu. *J. Chem. Phys.* **2010**, *132*, No. 154104.
(41) Leven, I.; Maaravi, T.; Azuri, I.; Kronik, L.; Hod, O. Interlayer Potential for Graphene/*h*-BN Heterostructures. *J. Chem. Theory Comput.* **2016**, *12*, 2896−2905.
(42) Ouyang, W.; Azuri, I.; Mandelli, D.; Tkatchenko, A.; Kronik, L.; Urbakh, M.; Hod, O. Mechanical and Tribological Properties of Layered Materials under High Pressure: Assessing the Importance of Many-Body Dispersion Effects. *J. Chem. Theory Comput.* **2020**, *16*, 666−676.
(43) Dietzel, D.; Brndiar, J.; Štich, I.; Schirmeisen, A. Limitations of Structural Superlubricity: Chemical Bonds versus Contact Size. *ACS Nano* **2017**, *11*, 7642−7647.
(44) Gaillac, R.; Pullumbi, P.; Coudert, F.-X. ELATE: An Open-Source Online Application for Analysis and Visualization of Elastic Tensors. *J. Phys.: Condens. Matter* **2016**, *28*, No. 275201.
(45) Lebedeva, I. V.; Knizhnik, A. A.; Popov, A. M.; Lozovik, Y. E.; Potapkin, B. V. Interlayer Interaction and Relative Vibrations of Bilayer Graphene. *Phys. Chem. Chem. Phys.* **2011**, *13*, 5687−5695.
(46) Reguzzoni, M.; Fasolino, A.; Molinari, E.; Righi, M. C. Potential Energy Surface for Graphene on Graphene: Ab Initio Derivation, Analytical Description, and Microscopic Interpretation. *Phys. Rev. B* **2012**, *86*, No. 245434.
(47) Liu, Y.; Wang, K.; Xu, Q.; Zhang, J.; Hu, Y.; Ma, T.; Zheng, Q.; Luo, J. Superlubricity between Graphite Layers in Ultrahigh Vacuum. *ACS Appl. Mater. Interfaces* **2020**, *12*, 43167−43172.
(48) Zhang, J.-J.; Dong, S. Superconductivity of Monolayer Mo_2C: The Key Role of Functional Groups. *J. Chem. Phys.* **2017**, *146*, No. 034705.
(49) Mannix, A. J.; Zhou, X.-F.; Kiraly, B.; Wood, J. D.; Alducin, D.; Myers, B. D.; Liu, X.; Fisher, B. L.; Santiago, U.; Guest, J. R.; Yacaman, M. J.; Ponce, A.; Oganov, A. R.; Hersam, M. C.; Guisinger, N. P. Synthesis of Borophenes: Anisotropic, Two-dimensional Boron Polymorphs. *Science* **2015**, *350*, 1513−1516.
(50) Castro Neto, A. H.; Guinea, F.; Peres, N. M. R.; Novoselov, K. S.; Geim, A. K. The Electronic Properties of Graphene. *Rev. Mod. Phys.* **2009**, *81*, 109−162.
(51) Splendiani, A.; Sun, L.; Zhang, Y.; Li, T.; Kim, J.; Chim, C.-Y.; Galli, G.; Wang, F. Emerging Photoluminescence in Monolayer MoS_2. *Nano Lett.* **2010**, *10*, 1271−1275.
(52) Liu, L.; Feng, Y. P.; Shen, Z. X. Structural and Electronic Properties of *h*-BN. *Phys. Rev. B* **2003**, *68*, No. 104102.
(53) Liu, D.; Luo, J. Chapter 9—Energy Dissipation through Phonon and Electron Behaviors of Superlubricity in 2D Materials. In

https://doi.org/10.1021/acsami.1c04870
ACS Appl. Mater. Interfaces XXXX, XXX, XXX−XXX

Superlubricity, 2nd ed.; Erdemir, A., Martin, J. M., Luo, J., Eds.; Elsevier, 2021, pp. 145−166.
(54) Carvalho, A.; Wang, M.; Zhu, X.; Rodin, A. S.; Su, H.; Castro Neto, A. H. Phosphorene: From Theory to Applications. *Nat. Rev. Mater.* **2016**, *1*, No. 16061.
(55) Liu, S.; Li, Z.; Ge, Y.; Wang, H.; Yue, R.; Jiang, X.; Li, J.; Wen, Q.; Zhang, H. Graphene/phosphorene Nano-heterojunction: Facile Synthesis, Nonlinear Optics, and Ultrafast Photonics Applications with Enhanced Performance. *Photonics Res.* **2017**, *5*, 662−668.
(56) Zhou, M.; Zhou, C.; Luo, K.; Li, W.; Liu, J.; Liu, Z.; Wu, Z. Ultrawide Bandwidth and Sensitive Electro-optic Modulator based on a Graphene Nanoelectromechanical System with Superlubricity. *Carbon* **2020**, *176*, 228−234.
(57) Li, H.; Wang, J.; Gao, S.; Chen, Q.; Peng, L.; Liu, K.; Wei, X. Superlubricity between MoS_2 Monolayers. *Adv. Mater.* **2017**, *29*, No. 1701474.
(58) Ozcelik, V. O.; Fathi, M.; Azadani, J. G.; Low, T. Tin Monochalcogenide Heterostructures as Mechanically Rigid Infrared Band Gap Semiconductors. *Phys. Rev. Mater.* **2018**, *2*, No. 051003(R).
(59) Woods, C. R.; Britnell, L.; Eckmann, A.; Ma, R. S.; Lu, J. C.; Guo, H. M.; Lin, X.; Yu, G. L.; Cao, Y.; Gorbachev, R. V.; Kretinin, A. V.; Park, J.; Ponomarenko, L. A.; Katsnelson, M. I.; Gornostyrev, Y. N.; Watanabe, K.; Taniguchi, T.; Casiraghi, C.; Gao, H. J.; Geim, A. K.; Novoselov, K. S. Commensurate−Incommensurate Transition in Graphene on Hexagonal Boron Nitride. *Nat. Phys.* **2014**, *10*, 451−456.
(60) Hohenberg, P.; Kohn, W. Inhomogeneous Electron Gas. *Phys. Rev.* **1964**, *136*, No. B864.
(61) Kohn, W.; Sham, L. J. Self-consistent Equations Including Exchange and Correlation Effects. *Phys. Rev.* **1965**, *140*, No. A1133.
(62) Kresse, G.; Furthmüller, J. Efficient Iterative Schemes for Ab Initio Total-Energy Calculations using a Plane-wave Basis Set. *Phys. Rev. B* **1996**, *54*, No. 11169.
(63) Blöchl, P. E. Projector Augmented-wave Method. *Phys. Rev. B* **1994**, *50*, No. 17953.
(64) Perdew, J. P.; Burke, K.; Ernzerhof, M. Generalized Gradient Approximation Made Simple. *Phys. Rev. Lett.* **1996**, *77*, 3865−3868.
(65) Klimeš, J.; Bowler, D. R.; Michaelides, A. Chemical Accuracy for the Van der Waals Density Functional. *J. Phys.: Condens. Matter* **2009**, *22*, No. 022201.
(66) Hamada, I. Van der Waals Density Functional Made Accurate. *Phys. Rev. B* **2014**, *89*, No. 121103(R).
(67) Steinmann, S. N.; Corminboeuf, C. Comprehensive Benchmarking of A Density-Dependent Dispersion Correction. *J. Chem. Theory Comput.* **2011**, *7*, 3567−3577.
(68) Monkhorst, H. J.; Pack, J. D. Special Points for Brillouin-Zone Integrations. *Phys. Rev. B* **1976**, *13*, No. 5188.
(69) Ramzan, M.; Li, Y.; Chimata, R.; Ahuja, R.; Chimata, R.; Ahuja, R. Electronic, Mechanical and Optical Properties of Y_2O_3 with Hybrid Density Functional (HSE06). *Comput. Mater. Sci.* **2013**, *71*, 19−24.
(70) Hajgató, B.; Güryel, S.; Dauphin, Y.; Blairon, J.-M.; Miltner, H. E.; Van Lier, G.; De Proft, F.; Geerlings, P. Theoretical Investigation of the Intrinsic Mechanical Properties of Single- and Double-layer Graphene. *J. Phys. Chem. C* **2012**, *116*, 22608−22618.

NOTE ADDED AFTER ASAP PUBLICATION

This paper was published on the Web on July 2, 2021. The Table of Contents/Abstract, Figure 4, and Supporting Information file were replaced, and the corrected version was reposted on July 7, 2021.

https://doi.org/10.1021/acsami.1c04870
ACS Appl. Mater. Interfaces XXXX, XXX, XXX−XXX

Supporting Information

Computational Prediction of Superlubric Layered Heterojunctions

Enlai Gao[#], Bozhao Wu[#], Yelingyi Wang, Xiangzheng Jia, Wengen Ouyang, and Ze Liu[*]

Department of Engineering Mechanics, School of Civil Engineering, Wuhan University, Wuhan, Hubei 430072, China.

[#]These authors contribute equally.

[*]Corresponding author. Email: ze.liu@whu.edu.cn.

This Supporting Information contains following sections:

1, Molecular dynamics simulation protocol

Molecular dynamics (MD) simulations using large-scale atomic/molecular massively parallel simulator (LAMMPS) computational package[1] were carried out to reveal the effect of binding energy on the interfacial friction of heterojunction. In all simulations, the aligned heterojunction graphene/hexagonal boron nitride (C_2/*h*-BN, $\theta = 0°$) with the size of $L \approx 136$ Å that is approximate to the size of Moiré pattern was used. Herein, we adopt the proposed simulation set-up by Song et al.[2]: The sliding graphene was dragged over the flat and rigid *h*-BN by a rigid duplicate of the sliding graphene layer that moves at a constant velocity of 10 m/s (Figure S1a); A classical harmonic spring was used to build connection between the atom of the sliding layer and the image atom of the duplicate layer. The in-plane interactions of the sliding graphene layer were described by using the reactive bond order (REBO) potential.[3] The interactions between the sliding and duplicate graphene layers were described by classical harmonic springs with the spring constant ($K_{||}$) of 11 meV/Å^2 in the lateral (x, y) directions for all carbon atoms.[2, 4] The interlayer interactions between the sliding graphene and the rigid *h*-BN substrate were described by the Lennard-Jones (L-J) potential, which is determined by the following form:

$$V_{ij} = 4\varepsilon\left[\left(\frac{\sigma}{r_{ij}}\right)^{12} - \left(\frac{\sigma}{r_{ij}}\right)^{6}\right]$$

where ε represents the potential well and σ represents the distance between carbon and nitrogen/boron atoms. In this work, the adopted L-J parameters (σ, ε) were taken from Ref.[5] as listed in Table S1. In all simulations, periodic boundary conditions (PBC) in lateral directions were employed. The Newton equations of motion were integrated using the Verlet algorithm with a time step of 1 fs. For each simulation, a full structural relaxation of the sliding monolayer using the FIRE algorithm[6] was first performed with a force criteria of 10^{-6} eV/Å. Afterwards, sliding simulations were performed by moving the rigid duplicate at a constant velocity V of 10 m/s along the zigzag (x) direction of the substrate. All simulations were performed at finite temperature (0.1 K) under the NVT ensemble with a time constant of 1 fs. The total simulation time is 2 ns. The average friction stress was calculated by time averaging the shear stress at

steady-state sliding (1.2–2.0 ns, Figure S1b). The instantaneous shear stress was calculated as F_K/A_{area}, where F_K is the lateral force of the duplicated graphene along the sliding direction, and A_{area} is the basal area of the sliding system. The amplitude of the interaction potential (U_{corr}) was defined as the difference of the maximum and minimum energy potential in the time range of 1.2–2.0 ns. To obtain the reliable results, each simulation was performed 6 times with different random numbers for the generating an ensemble of velocity at the specified temperature (0.1 K). The statistical errors can be calculated using 6 independent simulations. The effects of thermal fluctuations on the simulation results for the aligned graphene/*h*-BN heterojunction ($\theta = 0°$) have been investigated by Song et al.,[2] which indicate that the influence of thermal fluctuation (at temperatures up to 300 K) on the friction is quite small.

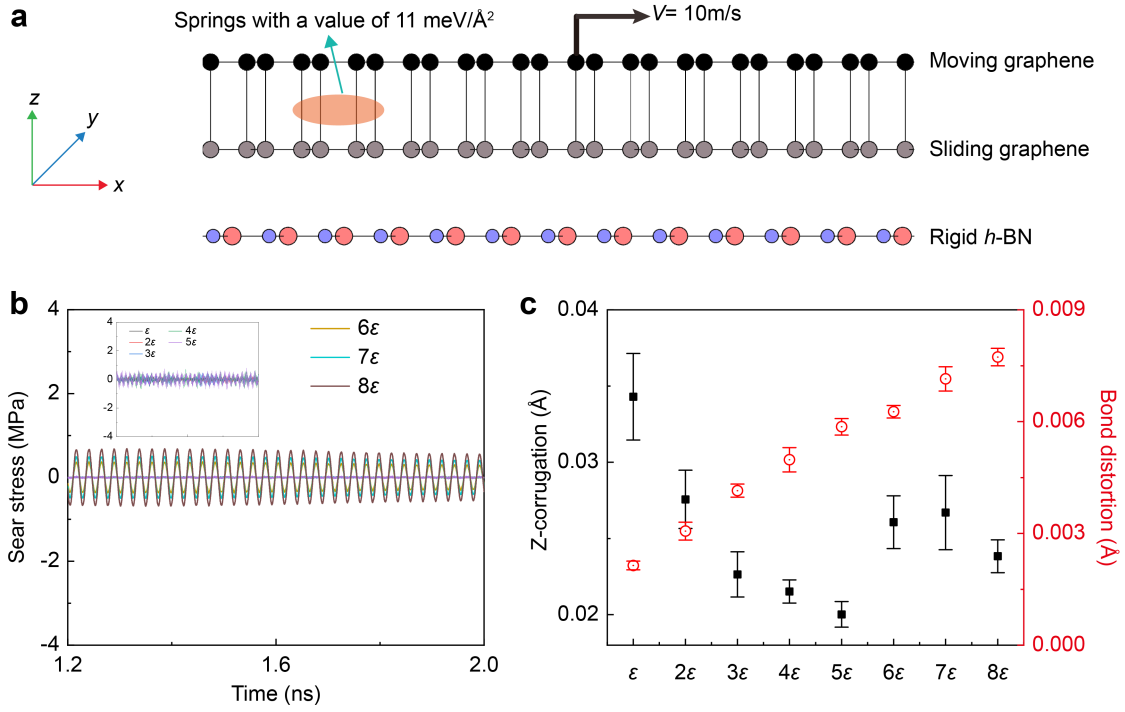

Figure S1. (a) Illustration of the simulation set-up. The sliding graphene layer moving over a rigid *h*-BN substrate is realized by dragging a rigid duplicate of the sliding graphene that moves at a constant velocity *V*. Each atom of the sliding graphene is connected to its image within the rigid duplicate via harmonic springs. With different interlayer interactions between the sliding graphene and rigid *h*-BN substrate, panel (b) shows the stimulated instantaneous shear stress at steady-state sliding (1.2–2.0 ns). All the results presented here were obtained using uniform

duplicate/graphene spring constants of $K_{\|}$ = 11 meV/Å^2 and a driving velocity of 10 m/s. (c) The out-of-plane [Δz = max(z_i) - min(z_i)] and local bond distortions [ΔL_{bond} = max($L_{\text{bond},\,i}$) - min($L_{\text{bond},\,i}$)] of the sliding graphene layer as a function of interlayer interactions were evaluated.

Table S1. Original and modified parameters of the L-J parameter (σ, ε) for the interlayer interactions between carbon, boron/nitrogen atoms.[5]

	Carbon-Boron	Carbon-Nitrogen
σ (Å)	3.41	3.37
ε (meV)	3.29	4.07
2ε (meV)	6.59	8.14
3ε (meV)	9.88	12.20
4ε (meV)	13.17	16.27
5ε (meV)	16.47	20.34
6ε (meV)	19.76	24.41
7ε (meV)	23.05	28.48
8ε (meV)	26.34	32.54

2, Rules of constructing heterojunction and different vdW dispersion corrections for the calculations of interlayer binding energy

As shown in the insets of Figure S2a, the co-incidence site lattice method[7] was used to construct the heterojunction. On the basis of two rules: (i) Minimizing the number of atoms in the unit cell of heterojunctions; (ii) Minimizing the mean misfit strain (ε_m) between two materials in a constructed heterojunction, in this work, ε_m is set to be less than 1%.[8, 9] Here, ε_m is calculated as $\varepsilon_m = (|\varepsilon_{11}|+|\varepsilon_{22}|+|\varepsilon_{12}|)/3$, where ε_{11} and ε_{22} are the in-plane normal strain along the base vectors of *a* and *b*, respectively, and ε_{12} is the in-plane shear strain of 2D cells. According to Figure S2a, The two rules balance the rationality of heterojunctions structures and the computational cost, e.g., the red point with ε_m of 0.89% and total atoms of 26 was used to determine the *h*-BN/2H-MoS_2 heterojunction with the relative orientation at twist angle ($\Delta\varphi$) of 19.11°.

To verify the reliability of the used vdW dispersion correction (DFT-D3)[10] for the calculations of the binding energy, other common vdW correction approaches of optB86b-vdW,[11] vdW-DF2[12] and DFT-dDsC[13] were also used for test, which agree with the DFT-D3 method (Figure S2b).

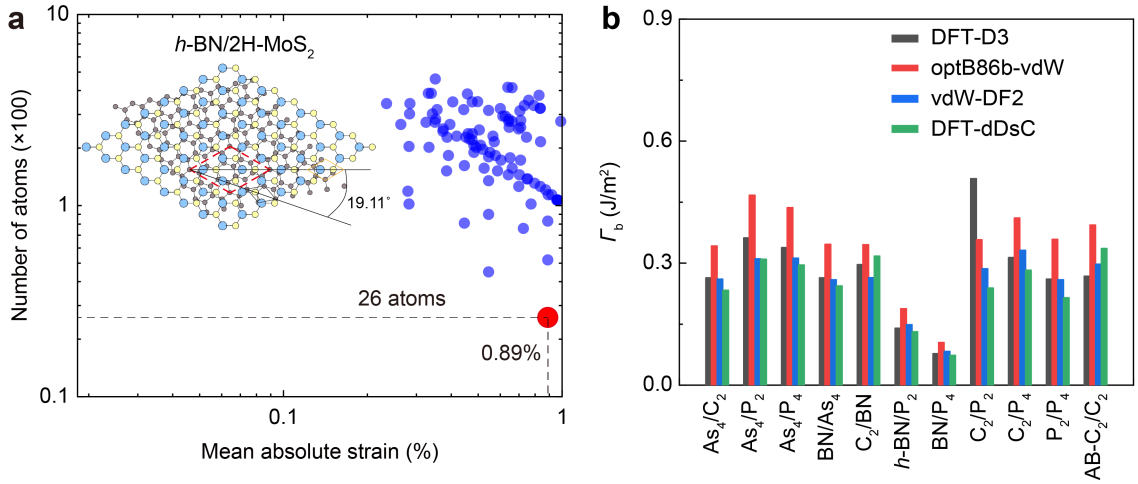

Figure S2. (a) Illustration of constructing heterojunctions using the co-incidence site lattice method,[7] e.g., *h*-BN/2H-MoS_2 with the relative orientation at twist angle ($\Delta\varphi$) of 19.11°. The marked red circle was determined by minimizing the number of atoms and mean misfit strain ($\varepsilon_m < 1\%$), which balance the rationality of heterojunctions structures and the computational cost. (b) Binding energies of typical heterojunctions by using different vdW correction methods.

3, Effects of high binding energy on the lattice deformation of heterojunction

As discussed in main text, there are 17 heterojunctions with high binding energy ($\Gamma_b > 1$ J/m^2). The high binding energy leads to a large vibration of atoms in the contact surfaces during sliding, which would result in local commensurate contact (a pinned state) and hence increasing the friction. For example, the Si_2/B_5 (1.04 J/m^2) and C_2/Sc_3C_2 (1.29 J/m^2) heterojuntions, their relaxed atomic configurations are shown in Figure S3. Compared with the initial configuratios, the high interlayer interactions cause a significant interatomic deformation and reduce the interlayer distances, which leads to the breaking of smooth surface.

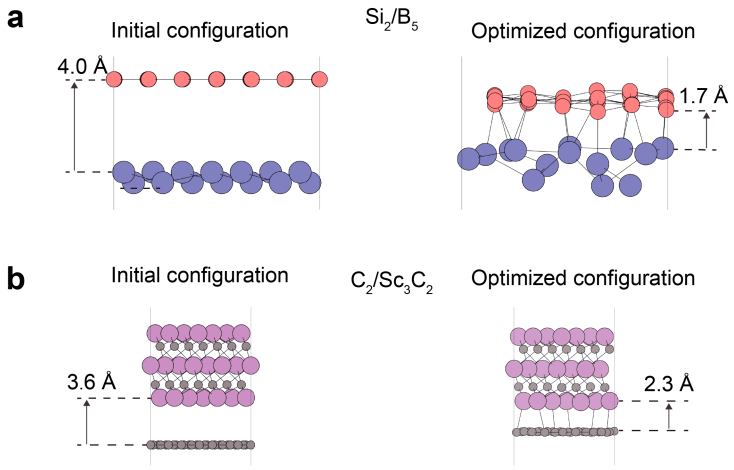

Figure S3. Side views of heterojunction configurations before (left) and after (right) structural optimization for the (a) Si_2B_5 and (b) C_2/Sc_3C_2 heterojunctions. The calculated binding energies were larger than 1 J/m^2, causing significant interatomic deformations and the reduced interlayer distances, and some chemical bonds have formed at the interfaces.

4, Effects of interlayer distances on the sliding PES and shear stress

To validate our first-principles calculation protocol,we perform benchmark tests for the bilayer graphene (AB stacking mode) configuration, as shown in the main test (Figure 5a and Figure S4a) with equlilibrium interlayer distance (*d*) of 3.52 Å on the basis of the DFT-D3 method. The obtained sliding potential energy surface (PES) is smaller than the previous work using the DFT-D method with the *d* of 3.25~3.31 Å,[14, 15] but close to the results using vdW-DF method with the *d* of 3.62 Å.[15] This difference is attributed to the different equilibrium interlayer distance (*d*) using different methods.[15] To clarify it, we did another two tests using the DFT-D3 method with the interlayer distances fixed at 3.31 and 3.2 Å, respectively, according the previous work.[15] As shown in Figure S4a, the obtained sliding barriers are in good agreement with that presented in Ref.[15] The deduced shear stress from the PES also increases with the decrease of *d* (Figure S4b).

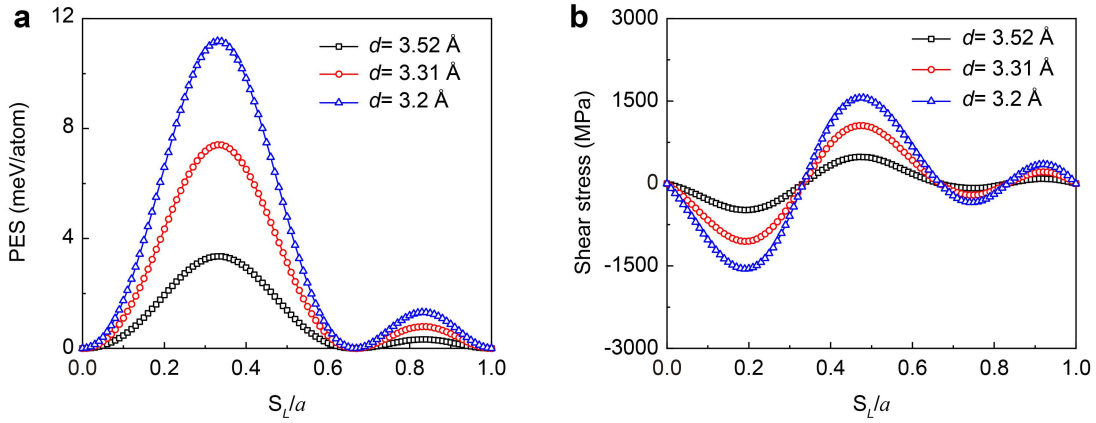

Figure S4. Calculated friction traces using first-principles calculations of bilayer graphene (AB stacking) along the armchair direction with different interlayer distances (*d*). (a) PES relative to the global energy minimum, and (b) the shear stress as a function of the sliding length (S_L) were obtained. *d* = 3.52 Å was the equilibrium distance obtained using the DFT-D3 method.

5, Heterojunction configurations used in the friction tests and the calculations of surface smoothness

As shown in Figure S5a-c, the optimized atomic configurations (top and side views) of heterojunctions correspond to the friction traces in Figure 5b-d. In addition, the friction test of the relaxed C_2/Sc_3C_2 heterojunction (Figure S3b) with binding energy (1.29 J/m^2) was also implemented (Figure 5e). The friction test was performed with the top layer sliding along the direction of the minimum in-plane stiffness (E_{min}). By comparing the in-plane stiffness of the 2D materials, the E_{min} of these heterojunctions (Figure S5 and Figure S3b) is from that of Sc_3C_2 and P_2, respectively. Considering the in-plane isotropic nature of Sc_3C_2 and P_2, the sliding direction was chosen along *a* direction of the lattice, corresponding to the *x* axis.

To investigate the surface smoothness, the altitude difference (Δh) along out-of-plane direction between atoms for the considered 2D materials were measured. As shown in Figure 2, the considered 2D materials can be divided into three categories with respect to the atomic layers: i), the single-atomic-layer structures (e.g, the graphene and *h*-BN); ii), the diatomic-layer structures (e.g., the P_2 and As_4); iii), polyatomic-layer structures (e.g, the 2H-MoS_2 and Sc_3C_2). For the multiatomic-layer and diatomic-layer structures (e.g., the Sc_3C_2 and P_2), the Δh is measured as the altitude difference between the surface and subsurface atoms as depicted in Figure S5a-b. For the single-atomic-layer structures (e.g, the graphene and *h*-BN), the Δh is zero. The measured Δh of these considered 2D materials is shown in Figure 5f in the main text.

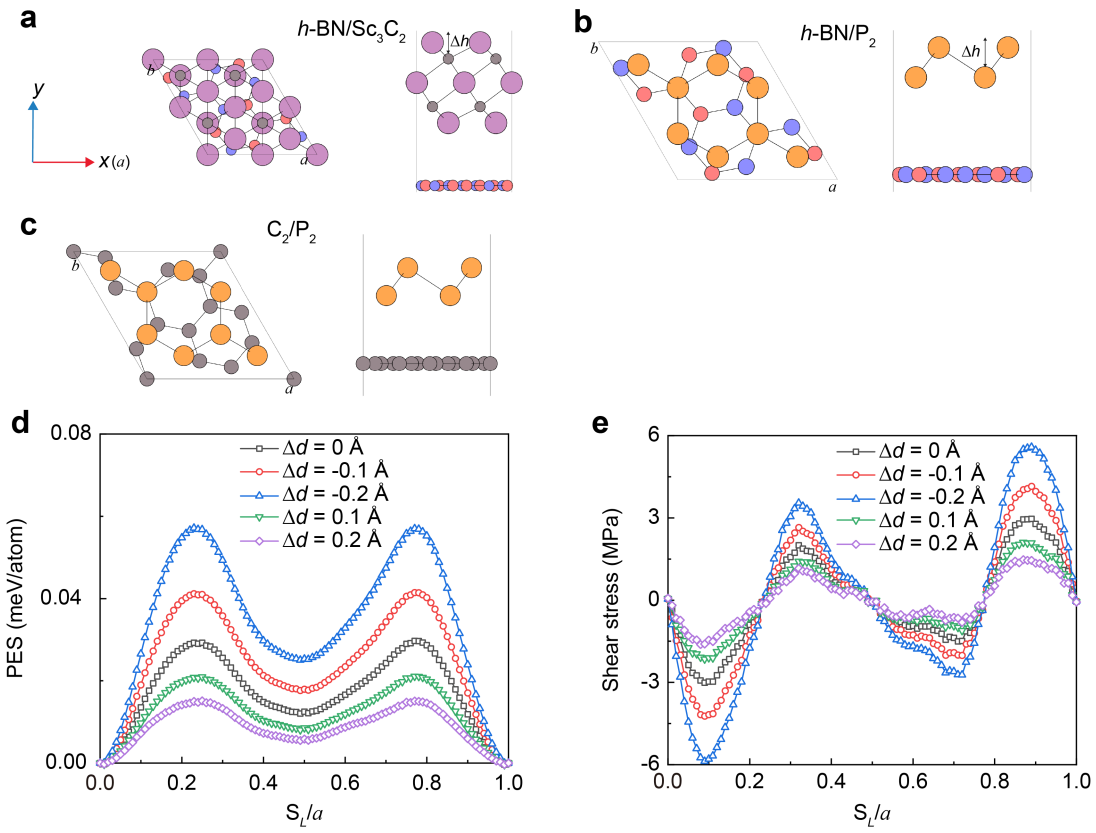

Figure S5. Top (left) and side (right) views of (a) *h*-BN/Sc_3C_2, (b) *h*-BN/P_2 and (c) C_2/P_2 heterojunctions for the calculations of friction traces using first-principles calculations, corresponding to the results shown in Figure 5b-d. The procedure was implemented by moving one layer sliding over the other layer along the *x* direction. Δh is the altitude difference along out-of-plane direction between atoms for considered 2D materials. (d-e) Calculated friction traces using first-principles calculations of the C_2/P_2 heterojunction with different interlayer distances. Δd is the change of layer spacing with respect to the equilibrium configuration. (d) PES relative to the global energy minimum, and (e) the shear stress as a function of the sliding length (S_L).

6, The influences of the relative orientation and sliding direction on the friction

Herein, we investigate the influence of the relative orientation.[2, 16-18] The relative orientation can be described by the misfit angle (θ) between the two layers in heterojunction. Since a large number of heterojunctions were considered in this work and it would be a huge task to systematically study these influences for each heterojunction. Herein, we take the C_2/P_2 heterojunction with different misfit angles as a case to investigate the influences of the relative orientation (Figure S6a). After structural optimizations, the friction traces using first-principles calculations were performed along the *x* direction. The obtained results of friction traces are shown in Figure S6c-d. The results of friction trace of the C_2/P_2 with the misfit angle of 19.11° has been shown in Figure 5d. The statistics average friction stress for the four heterojunctions shows in Figure S7a, demonstrating that the average friction stress decreases (9.90-1.46 MPa) with the increase of the misfit angle. This phenomenon has also been observed in previous work on graphene/*h*-BN heterojunction.[2, 19, 20]

On the other hand, the influence of the sliding direction between the sliding layers is also of importance. We take the C_2/P_2 heterojunction with the misfit angle of 19.11° as an example to investigate the influence of the sliding direction on the friction. First, the sliding was performed along the *y* direction (Figure S5c) with a sliding step of $\Delta S_L/b^*=0.1$ (b^* represents the period length of the 2D heterojunction lattice along the *y* direction). Then ten structures at equal intervals along the *y* direction were obtained. Starting with the each obtained structure, the sliding along the *x* direction with a sliding step of $\Delta S_L/a=0.01$ was performed. Finally, a thousand sliding points in the area at the interface between C_2 and P_2 were obtained. The obtained sliding PES was illustrated in Figure S7b, showing that the maximum sliding energy barrier is 0.0325 meV/atom that is only slightly larger than that (0.0297 meV/atom) in Figure 5d. This result indicates that the influence of the sliding direction on friction trace of is quite small.

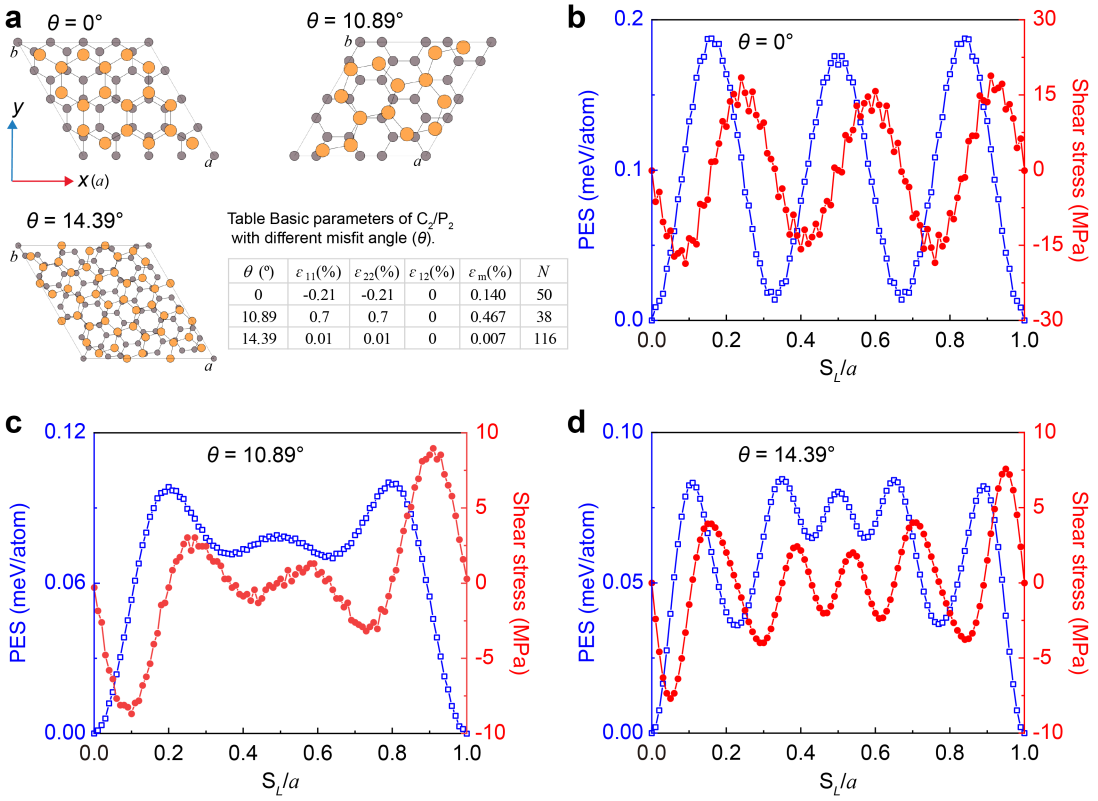

Figure S6. (a) Top views of the C_2/P_2 heterojunctions with the misfit angles of 0°, 10.89°, and 14.39°. The inset table in panel (a) gives the basic parameters for constructing C_2/P_2 heterojunctions. The corresponding calculated friction traces were shown in (b-d). The procedure was implemented by moving one layer sliding over the other layer along the *x* direction, respectively.

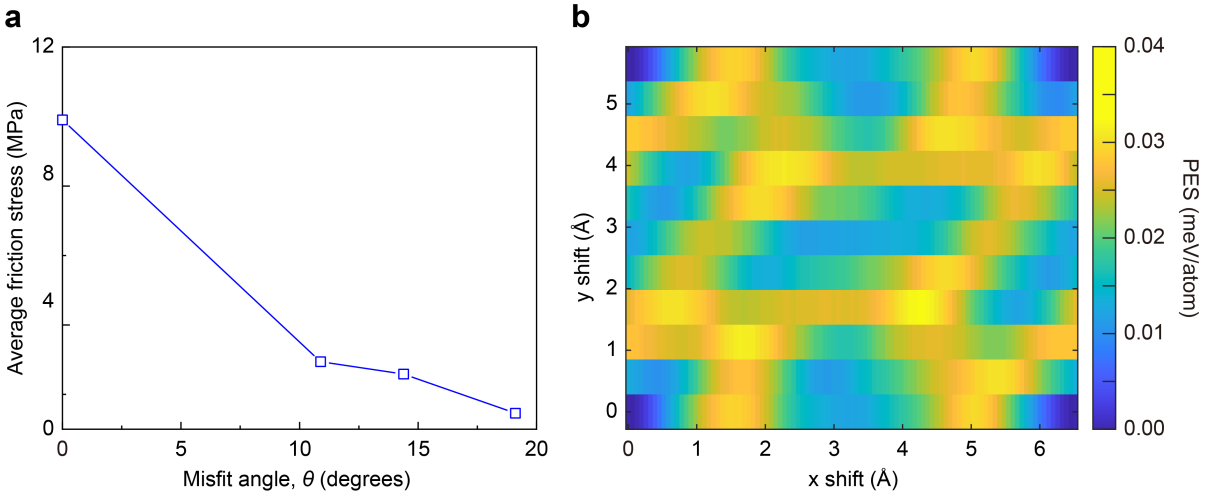

Figure S7. Influences of (a) the relative orientation and (b) sliding direction between the C_2/P_2 heterojunction.

Table S2. Γ_b, E_{min}, E_{min}/Γ_b, ε_m, ε_{11}, ε_{22}, ε_{12} and the total atoms (N) of 2D heterojunctions, and C_2/C_2 and MoS_2/MoS_2 bilayer.

	Γ_b	E_{min}	E_{min}/Γ_b	ε_{11}	ε_{22}	ε_{12}	ε_m	N
C_2-AB	0.27	340.47	1266.4	/	/	/	/	4
C_2/*h*-BN	0.30	275.07	927.5	-0.91	-0.91	0.00	0.61	4
h-BN/Sc_3C_2	0.24	155.29	645.7	0.87	0.87	0.00	0.58	34
h-BN/B_4	0.24	155.84	641.0	0.19	-0.17	0.03	0.13	76
h-BN/B_5	0.26	165.15	638.4	0.49	-0.42	0.00	0.30	31
h-BN/Ti_3C_2	0.36	224.18	629.3	1.29	1.29	0.00	0.86	71
C_2/Mo_2C	0.19	115.58	624.7	-0.05	-0.05	0.00	0.03	34
C_2/B_4	0.28	155.84	566.0	-0.81	-0.88	-0.01	0.57	44
h-BN/P_2	0.14	77.50	554.0	-0.72	-0.72	0.00	0.48	22
C_2/B_5	0.30	165.15	541.7	1.39	-1.32	0.00	0.90	31
C_2/B_2	0.30	160.00	525.2	0.48	0.22	0.59	0.43	30
C_2/Ti_2C	0.35	130.61	369.5	1.13	-1.13	0.00	0.75	53
h-BN/Ti_2C	0.35	130.61	368.3	0.24	0.24	0.00	0.16	53
h-BN/2H-MoS_2	0.35	126.01	363.1	0.27	0.27	0.00	0.18	74
Ga_2S_2/P_2	0.22	77.40	358.9	1.26	1.26	0.00	0.84	92
2H-MoS_2/B_4	0.35	126.01	358.0	0.00	-0.07	-0.01	0.03	41
Ga_2S_2-3/P_2	0.22	74.30	344.9	1.12	1.12	0.00	0.75	92
h-BN/B_2	0.47	160.00	338.2	-0.14	0.36	0.68	0.39	26
Ga_2S_2/*h*-BN	0.24	78.87	331.9	0.05	0.05	0.00	0.03	98
Ga_2Se_2/Ga_2S_2	0.20	66.10	324.5	0.35	0.55	1.30	0.73	168
Ga_2Se_2/Ga_2S_2-3	0.21	66.10	320.4	-0.34	-0.43	1.32	0.70	168
Ga_2S_2-3/*h*-BN	0.24	74.30	312.5	-0.09	-0.09	0.00	0.06	98
2H-MoS_2/B_5	0.41	126.01	305.1	1.06	-1.10	0.03	0.73	79
Ga_2S_2-3/Bi_2Se_3	0.20	61.42	301.6	-0.42	-0.42	0.00	0.28	62
Ga_2S_2/Ga_2S_2-3	0.25	74.30	296.5	0.14	0.14	0.00	0.09	16
P_2/B_5	0.27	77.40	288.9	-0.45	-0.42	-0.03	0.30	66
2H-MoS_2-AB	0.44	126.01	287.4	0.00	0.00	0.00	0.00	6
Ga_2Se_2/*h*-BN	0.23	66.10	286.0	-0.50	-0.50	0.00	0.33	34

h-BN/P_4	0.08	21.85	282.4	-0.38	0.96	-1.29	0.88	38
Ga_2Se_2/P_2	0.24	66.10	279.7	-0.31	0.31	0.00	0.21	40
P_2/B_4	0.28	77.40	276.9	1.26	-1.32	0.02	0.87	26
Ga_2S_2-3/C_2	0.27	74.30	274.9	0.93	0.93	0.00	0.62	34
Ga_2S_2/Bi_2Se_3	0.22	61.42	274.4	-0.28	-0.28	0.00	0.19	62
P_2/2H-MoS_2	0.29	77.40	268.1	0.49	0.49	0.00	0.33	63
h-BN/1T-MoS_2	0.34	90.90	265.6	0.29	0.29	0.00	0.19	74
Bi_2Te_3/C_2	0.19	49.87	263.5	0.33	0.33	0.00	0.22	46
Ga_2Se_2/Bi_2Se_3	0.23	61.42	261.8	0.13	-1.02	-1.02	0.72	232
Bi_2Se_3/*h*-BN	0.24	61.42	261.0	0.60	-2.26	0.00	0.95	128
Bi_2Se_3/P_2	0.24	61.42	257.0	-0.44	0.08	-2.27	0.93	82
Ga_2Se_2/C_2	0.26	66.10	256.3	-1.41	-1.41	0.00	0.94	34
Bi_2Se_3/C_2	0.24	61.42	256.2	1.35	-1.35	0.00	0.90	22
C_2/1T-MoS_2	0.36	90.90	254.6	-1.32	-1.32	0.00	0.88	26
Ga_2Te_2/Ga_2S_2-3	0.21	53.60	253.2	0.76	0.76	0.00	0.51	56
P_2/1T-MoS_2	0.31	77.40	251.8	0.50	0.50	0.00	0.33	63
Ga_2Te_2/Ga_2S_2	0.21	53.60	250.0	0.62	0.62	0.00	0.41	56
C_2/Si_2	0.25	61.39	245.5	1.28	1.28	0.00	0.85	20
Ga_2Te_2/*h*-BN	0.22	53.60	244.4	-1.14	-1.14	0.00	0.76	110
h-BN/Mo_2C	0.48	115.58	241.3	-0.04	0.04	0.00	0.03	39
h-BN/Si_2	0.26	61.39	240.7	0.38	0.38	0.00	0.25	20
Bi_2Te_3/P_2	0.21	49.87	238.0	-0.97	0.97	0.00	0.65	34
Ga_2Te_2/C_2	0.23	53.60	236.7	-0.81	-0.81	0.00	0.54	132
Ga_2Se_2/Bi_2Te_3	0.22	49.87	231.4	0.26	0.26	0.00	0.17	62
Ga_2Te_2/P_2	0.23	53.60	231.1	-0.11	-0.11	0.00	0.07	86
Bi_2Te_3/*h*-BN	0.23	49.87	221.5	0.77	-0.77	0.00	0.51	22
C_2/2H-MoS_2	0.58	126.01	218.1	-1.33	-1.33	0.00	0.89	26
Ga_2S_2-3/Bi_2Te_3	0.23	49.87	217.5	0.60	0.60	0.00	0.40	194
Ga_2S_2/Bi_2Te_3	0.23	49.87	217.4	0.74	0.74	0.00	0.49	194
P_2/Si_2	0.29	61.39	209.4	1.10	1.10	0.00	0.73	14
P_2/B_2	0.37	77.40	209.0	0.64	-0.74	0.00	0.46	12

Bi_2Te_3/Bi_2Se_3	0.25	49.87	198.8	-0.19	-1.09	-1.30	0.86	210
Ga_2Te_2/Bi_2Se_3	0.29	53.60	182.2	0.33	0.33	0.00	0.22	18
Cu_2I_2/Bi_2Se_3	0.21	32.89	160.4	0.17	0.17	0.00	0.11	18
C_2/P_2	0.51	77.40	152.7	0.19	0.19	0.00	0.13	22
Cu_2I_2/*h*-BN	0.23	32.89	141.1	-1.31	-1.31	0.00	0.87	110
Si_2/1T-MoS_2	0.45	61.39	135.7	-0.30	-0.30	0.00	0.20	83
Si_2/2H-MoS_2	0.45	61.39	135.7	-0.32	-0.32	0.00	0.21	83
Ga_2S_2/Cu_2I_2	0.25	32.89	133.4	-0.45	-0.45	0.00	0.30	56
Ga_2S_2-3/Cu_2I_2	0.25	32.89	132.2	-0.60	-0.60	0.00	0.40	56
Ga_2Se_2/Cu_2I_2	0.25	32.89	132.1	0.80	0.00	1.04	0.61	208
Cu_2I_2/C_2	0.25	32.89	131.2	-0.98	-0.98	0.00	0.65	132
Bi_2/C_2	0.20	25.15	126.1	-0.71	0.71	0.00	0.47	8
Cu_2I_2/Bi_2Te_3	0.26	32.89	126.1	0.37	-1.27	-1.30	0.98	188
Cu_2I_2/P_2	0.27	32.89	121.8	-0.27	0.25	-2.27	0.93	72
$Cu_2Te_2/CdCl_2$	0.20	24.30	120.4	1.10	-0.87	0.00	0.66	58
C_2/Sc_3C_2	1.29	155.29	120.1	0.28	-0.28	0.00	0.19	61
$Ga_2S_2/CdCl_2$	0.22	25.50	118.1	-0.48	-1.37	-1.02	0.96	180
Ga_2S_2-3/$CdCl_2$	0.22	25.50	117.8	1.36	1.36	0.00	0.91	110
C_2/Ti_3C_2	1.91	224.18	117.5	0.22	0.22	0.00	0.15	98
$CdCl_2/Bi_2Te_3$	0.22	25.50	116.4	0.72	0.72	0.00	0.48	82
$Ga_2Se_2/CdCl_2$	0.23	25.50	110.5	-0.07	0.07	0.00	0.05	48
h-BN/Bi_2	0.23	25.15	109.6	-0.20	-0.20	0.00	0.13	8
Ga_2Te_2/Bi_2	0.24	25.15	106.2	-0.44	-0.47	-1.30	0.74	128
Cu_2Te_2/*h*-BN	0.23	24.30	105.8	-2.16	0.59	-0.09	0.95	60
Bi_2/P_2	0.25	25.15	102.2	-0.01	-0.01	0.00	0.01	22
1T-MoS_2/B_2	0.89	90.897	101.7	0.76	-2.14	0.00	0.97	7
$CdCl_2$/*h*-BN	0.26	25.50	100.0	0.47	0.47	0.00	0.31	26
$CdCl_2/P_2$	0.26	25.50	99.9	-0.24	-0.25	0.00	0.16	10
Cu_2Te_2/C_2	0.25	24.30	98.6	0.03	-2.17	0.00	0.73	82
Ga_2S_2/Bi_2	0.26	25.15	98.5	-0.22	-0.22	0.00	0.15	140
Ga_2S_2-3/Bi_2	0.26	25.15	97.0	-0.36	-0.36	0.00	0.24	140

Ga_2S_2-3/Cu_2Te_2	0.26	24.30	94.3	2.25	0.57	-0.12	0.98	92
$CdCl_2/C_2$	0.27	25.50	92.9	-0.43	-0.43	0.00	0.29	26
2H-MoS_2/B_2	1.44	126.01	87.8	2.15	-0.77	0.00	0.97	14
Si_2/B_4	0.70	61.391	87.3	2.12	0.20	-0.29	0.87	64
Ga_2Te_2/CaI_2	0.19	16.58	86.5	1.12	0.22	-1.30	0.88	146
Cu_2Te_2/P_4	0.28	24.30	86.3	0.96	-1.81	0.00	0.92	44
Ga_2Se_2/Bi_2	0.29	25.15	85.6	-0.70	-0.70	0.00	0.47	22
Ga_2S_2-3/CaI_2	0.20	16.58	84.9	1.27	0.47	1.04	0.93	184
P_2/P_4	0.26	21.85	83.9	-0.87	-0.05	-0.28	0.40	44
Ga_2Te_2/Cu_2I_2	0.29	24.30	82.9	0.16	0.16	0.00	0.11	16
$CdCl_2/P_4$	0.26	21.85	82.8	0.09	0.54	0.00	0.21	78
$CdCl_2/CaI_2$	0.20	16.58	82.5	0.45	0.45	0.00	0.30	132
Ga_2Se_2/Cu_2Te_2	0.30	24.30	82.2	-0.07	-1.42	1.16	0.88	112
Bi_2Te_3/P_4	0.27	21.85	81.7	-0.20	1.10	-1.60	0.97	112
Ga_2S_2/Cu_2Te_2	0.30	24.30	81.6	2.39	0.43	-0.12	0.98	92
Cu_2Te_2/P_2	0.30	24.30	81.6	0.62	-0.15	-2.05	0.94	34
CaI_2/*h*-BN	0.20	16.58	81.0	-0.57	-0.57	0.00	0.38	98
Ga_2Te_2/Cu_2Te_2	0.30	24.30	80.3	-0.09	-0.07	2.32	0.83	120
Cu_2Te_2/Cu_2I_2	0.30	24.30	79.8	-0.46	-0.08	2.24	0.93	52
Ga_2Se_2/CaI_2	0.21	16.58	79.3	0.38	-0.38	1.32	0.69	148
Ga_2Se_2/P_4	0.28	21.85	78.9	0.03	-1.57	0.00	0.53	72
CaI_2/Bi_2Te_3	0.21	16.58	78.0	-1.21	1.21	0.00	0.81	124
Cu_2I_2/CaI_2	0.21	16.58	77.2	0.12	-0.89	1.32	0.78	146
Ga_2S_2-3/P_4	0.28	21.85	76.8	-0.62	0.53	1.62	0.92	84
CaI_2/Bi_2Se_3	0.22	16.58	75.2	0.05	-0.72	1.32	0.70	166
Bi_2Se_3/P_4	0.29	21.85	74.9	-1.05	-1.80	-0.01	0.95	72
CaI_2/C_2	0.22	16.58	74.3	-0.34	-0.34	0.00	0.23	98
Cu_2Br_2/Au_2Br_2	0.11	7.84	72.4	0.02	0.00	0.68	0.23	68
Bi_2Se_3/Bi_2	0.35	25.15	71.8	0.06	-0.70	1.32	0.69	150
CaI_2/Bi_2	0.23	16.58	71.7	-1.08	-1.08	0.00	0.72	74
CaI_2/P_2	0.23	16.58	71.5	1.27	1.27	0.00	0.85	98

C_2/P_4	0.31	21.85	69.7	-0.40	-1.30	-0.05	0.58	58
Bi_2Te_3/Bi_2	0.37	25.15	67.2	-0.96	-0.96	0.00	0.64	14
Ga_2Te_2/P_4	0.33	21.85	65.9	-0.71	-2.14	-0.01	0.95	64
Cu_2Te_2/Bi_2	0.37	24.30	65.4	-0.35	-0.83	-0.15	0.44	84
Bi_2/P_4	0.34	21.85	64.2	1.14	-0.81	0.05	0.67	82
CaI_2/P_4	0.26	16.58	63.6	-0.46	-0.04	1.99	0.83	66
Cu_2I_2/P_4	0.35	21.85	63.1	-0.88	-1.97	-0.01	0.95	64
Cu_2Te_2/CaI_2	0.27	16.58	62.1	-2.57	0.10	0.00	0.89	60
Si_2/B_5	1.04	61.391	59.0	-0.42	-0.46	-0.03	0.30	44
Ga_2S_2/Au_2Br_2	0.20	11.00	54.8	0.41	2.21	0.00	0.87	104
Au_2Br_2/*h*-BN	0.20	11.00	54.7	0.02	-1.93	0.66	0.87	32
Sc_3C_2/B_2	2.87	155.29	54.1	0.96	0.21	0.36	0.51	56
CaI_2/Au_2Br_2	0.21	11.00	52.4	-0.06	0.02	1.83	0.64	86
Au_2Br_2/C_2	0.21	11.00	51.7	-0.92	1.02	-0.66	0.87	32
Au_2Br_2/P_2	0.22	11.00	50.8	-1.04	1.32	0.25	0.87	38
Ga_2Te_2/Au_2Br_2	0.22	11.00	50.3	-0.15	-0.41	1.17	0.58	44
Cu_2I_2/Au_2Br_2	0.22	11.00	50.0	-1.40	0.51	0.69	0.87	44
$CdCl_2/Au_2Br_2$	0.22	11.00	49.0	1.22	-0.65	0.00	0.62	94
Ga_2Se_2/Au_2Br_2	0.23	11.00	48.8	-1.38	-0.62	-0.72	0.91	108
Bi_2Se_3/Au_2Br_2	0.24	11.00	46.3	-1.57	0.34	0.69	0.87	50
Cu_2Br_2/CaI_2	0.17	7.84	46.2	1.23	0.34	-0.18	0.58	92
Au_2Br_2/P_4	0.24	11.00	45.8	2.21	0.22	0.42	0.95	44
Bi_2Te_3/Au_2Br_2	0.24	11.00	45.7	-0.84	-0.56	0.25	0.55	140
P_2/Sc_3C_2	1.86	77.40	41.7	-0.42	-0.42	0.00	0.28	86
$CdCl_2/Au_2Se_2$	0.22	8.78	40.1	-1.44	0.09	1.41	0.98	40
h-BN/As_4	0.26	10.40	39.5	1.15	-0.15	-0.11	0.47	92
As_4/C_2	0.26	10.40	39.4	2.14	-0.39	0.00	0.84	76
Au_2Br_2/As_4	0.26	10.40	39.4	0.02	-0.26	-2.34	0.87	48
Cu_2Br_2/*h*-BN	0.20	7.84	39.3	0.98	-0.94	0.96	0.96	46
Cu_2I_2/Cu_2Br_2	0.20	7.84	38.6	-0.16	-0.13	-0.96	0.42	140
Cu_2Br_2/C_2	0.20	7.84	38.5	0.08	-0.04	0.96	0.36	48

Ti_3C_2/B_2	4.25	160.00	37.6	0.40	-1.60	0.80	0.93	68
CaI_2/As_4	0.28	10.40	37.0	0.27	-1.11	0.77	0.72	110
Cu_2Te_2/Au_2Br_2	0.30	11.00	36.8	0.73	0.27	0.10	0.37	112
Au_2Br_2/Bi_2	0.30	11.00	36.8	0.12	-2.01	-0.57	0.90	50
$CdCl_2/As_4$	0.28	10.40	36.5	0.32	-1.30	-0.28	0.63	94
Ga_2S_2-3/Cu_2Br_2	0.22	7.84	35.5	1.84	0.09	0.00	0.64	64
Cu_2Br_2/P_2	0.22	7.84	35.2	-0.52	1.01	0.59	0.71	58
Ga_2Se_2/Au_2Se_2	0.25	8.78	34.6	-1.50	0.02	1.41	0.98	40
Bi_2Se_3/Au_2Se_2	0.26	8.78	34.0	-0.58	0.64	1.45	0.89	82
Ga_2S_2/Cu_2Br_2	0.23	7.84	33.9	0.05	-1.98	0.00	0.68	64
Ga_2S_2/As_4	0.31	10.40	33.6	0.95	0.23	0.00	0.39	40
Ga_2S_2-3/As_4	0.31	10.40	33.6	0.81	0.09	0.00	0.30	40
Ga_2Te_2/As_4	0.31	10.40	33.1	-0.03	0.78	1.62	0.81	88
Cu_2I_2/As_4	0.32	10.40	33.0	-0.20	0.94	1.62	0.92	88
Cu_2I_2/Au_2Se_2	0.27	8.78	33.0	-0.09	-2.66	-0.09	0.95	104
CaI_2/Au_2Se_2	0.27	8.78	32.5	-1.52	-1.16	0.00	0.89	24
Si_2/Mo_2C	1.89	61.39	32.4	-1.33	-1.33	0.00	0.89	29
Bi_2Se_3/As_4	0.33	10.40	31.3	0.32	-0.39	0.00	0.24	118
Si_2/B_2	1.98	61.391	31.0	-1.84	-0.46	0.00	0.77	22
As_4/P_4	0.34	10.40	30.8	2.27	-0.04	0.00	0.77	88
Si_2/Ti_2C	2.05	61.39	30.0	-0.14	-0.14	0.00	0.09	89
Bi_2Te_3/As_4	0.35	10.40	29.8	0.18	-1.40	-0.13	0.57	90
Ga_2Se_2/As_4	0.35	10.40	29.8	0.26	-1.85	-0.28	0.80	112
Ti_2C/B_2	4.48	130.61	29.1	0.27	-1.65	0.00	0.64	92
As_4/P_2	0.36	10.40	28.8	-0.96	-1.15	-0.55	0.89	38
Si_2/Sc_3C_2	2.15	61.39	28.6	0.48	0.48	0.00	0.32	52
Cu_2Te_2/As_4	0.37	10.40	28.2	-0.27	0.51	1.05	0.61	76
P_2/Mo_2C	2.75	77.40	28.2	0.16	-0.16	0.00	0.11	36
As_4/Bi_2	0.38	10.40	27.6	1.52	0.86	0.13	0.84	50
P_2/Ti_3C_2	2.86	77.40	27.1	-0.79	-0.79	0.00	0.53	89
Cu_2Br_2/P_4	0.29	7.84	27.1	-0.49	-1.88	0.00	0.79	28

Cu_2Br_2/As_4	0.39	10.40	27.0	-0.66	0.69	-0.99	0.78	88
Mo_2C/B_2	4.71	115.58	24.5	0.48	-0.90	0.00	0.46	12
P_2/Ti_2C	3.16	77.40	24.5	0.45	-0.45	0.00	0.30	89
Au_2Se_2/*h*-BN	0.46	8.78	19.0	-2.01	-0.75	-0.09	0.95	76
Si_2/Ti_3C_2	3.55	61.39	17.3	0.81	0.81	0.00	0.54	119
Au_2Se_2/C_2	0.54	8.78	16.3	0.42	1.39	0.83	0.88	54
Au_2Se_2/As_4	0.57	8.78	15.5	1.05	0.65	-0.43	0.71	100
Au_2Se_2/Au_2Br_2	0.62	8.78	14.1	-0.24	-1.82	-0.53	0.86	80
Au_2Se_2/P_2	0.65	8.78	13.5	0.90	0.05	-0.11	0.35	88
Au_2Se_2/P_4	0.65	8.78	13.4	-0.84	0.77	0.00	0.54	44
Ag_2I_2/C_2	0.15	1.90	12.8	0.60	1.33	0.00	0.64	68
Ag_2I_2/*h*-BN	0.16	1.90	12.2	0.42	-1.50	0.00	0.64	68
Bi_2Te_3/Au_2Se_2	0.73	8.78	12.1	-2.78	0.02	-0.09	0.96	68
CaI_2/Ag_2I_2	0.16	1.90	11.6	-0.14	1.78	0.00	0.64	94
Cu_2Br_2/Ag_2I_2	0.17	1.90	11.4	1.01	1.01	0.00	0.67	36
Ag_2I_2/P_2	0.17	1.90	10.9	0.47	-1.53	0.95	0.98	78
Ga_2Se_2/Ag_2I_2	0.18	1.90	10.7	-0.39	1.53	-0.94	0.95	108
Cu_2I_2/Ag_2I_2	0.19	1.90	10.0	-0.61	-0.09	0.00	0.23	88
Au_2Se_2/Bi_2	0.90	8.78	9.8	-0.95	-1.81	0.09	0.95	44
Ag_2I_2/P_4	0.19	1.90	9.8	-0.43	-0.21	-1.18	0.61	64
Au_2Br_2/Ag_2I_2	0.20	1.90	9.7	0.96	0.29	-0.26	0.50	88
Bi_2Te_3/Ag_2I_2	0.20	1.90	9.6	0.29	-1.86	0.18	0.78	124
Ga_2Te_2/Ag_2I_2	0.20	1.90	9.5	0.07	-1.99	0.00	0.69	64
Cu_2Te_2/Ag_2I_2	0.20	1.90	9.4	0.38	0.59	1.16	0.71	48
Bi_2Se_3/Ag_2I_2	0.21	1.90	9.0	0.39	-0.40	2.05	0.95	88
Ag_2I_2/As_4	0.23	1.90	8.2	0.08	0.89	0.08	0.35	100
Au_2Se_2/Ag_2I_2	0.85	1.90	2.2	-0.51	0.32	-0.60	0.48	68

REFERENCES

1. Plimpton, S., Fast Parallel Algorithms for Short-range Molecular Dynamics. *Journal of Computational Physics* **1995,** *117* (1), 1-19.
2. Song, Y.; Mandelli, D.; Hod, O.; Urbakh, M.; Ma, M.; Zheng, Q., Robust Microscale Duperlubricity in Graphite/Hexagonal Boron Nitride Layered Heterojunctions. *Nature Materials* **2018,** *17* (10), 894-899.
3. Brenner, D. W.; Shenderova, O. A.; Harrison, J. A.; Stuart, S. J.; Ni, B.; Sinnott, S. B., A Second-generation Reactive Empirical Bond Order (REBO) Potential Energy Expression for Hydrocarbons. *Journal of Physics: Condensed Matter* **2002,** *14* (4), 783-802.
4. Kolmogorov, A. N.; Crespi, V. H., Registry-Dependent Interlayer Potential for Graphitic Systems. *Physical Review B* **2005,** *71* (23), 235415.
5. Iwata, T.; Shintani, K., Reduction of the Thermal Conductivity of a Graphene/*h*-BN Heterobilayer via Interlayer sp^3 Bonds. *Physical Chemistry Chemical Physics* **2018,** *20* (7), 5217-5226.
6. Bitzek, E.; Koskinen, P.; Gähler, F.; Moseler, M.; Gumbsch, P., Structural Relaxation Made Simple. *Physical Review Letters* **2006,** *97* (17), 170201.
7. Koda, D. S.; Bechstedt, F.; Marques, M.; Teles, L. K., Coincidence Lattices of 2D Crystals: Heterostructure Predictions and Applications. *The Journal of Physical Chemistry C* **2016,** *120* (20), 10895-10908.
8. Zur, A.; McGill, T. C., Lattice Match: An Application to Heteroepitaxy. *Journal of Applied Physics* **1984,** *55* (2), 378-386.
9. Liu, J.; Cheng, B.; Yu, J., A New Understanding of the Photocatalytic Mechanism of the Direct Z-scheme g-C_3N_4/TiO_2 Heterostructure. *Physical Chemistry Chemical Physics* **2016,** *18* (45), 31175-31183.
10. Grimme, S.; Antony, J.; Ehrlich, S.; Krieg, H., A Consistent and Accurate Ab Initio Parametrization of Density Functional Dispersion Correction (DFT-D) for the 94 Elements H-Pu. *The Journal of Chemical Physics* **2010,** *132* (15), 154104.
11. Klimeš, J.; Bowler, D. R.; Michaelides, A., Chemical Accuracy for the Van der Waals Density Functional. *Journal of Physics: Condensed Matter* **2009,** *22* (2), 022201.
12. Hamada, I., Van der Waals Density Functional Made Accurate. *Physical Review B* **2014,** *89* (12), 121103(R).
13. Steinmann, S. N.; Corminboeuf, C., Comprehensive Benchmarking of a Density-Dependent Dispersion Correction. *Journal of Chemical Theory and Computation* **2011,** *7* (11), 3567-3577.
14. Lebedeva, I. V.; Knizhnik, A. A.; Popov, A. M.; Lozovik, Y. E.; Potapkin, B. V., Interlayer Interaction and Relative Vibrations of Bilayer Graphene. *Physical Chemistry Chemical Physics* **2011,** *13* (13), 5687-5695.

15. Reguzzoni, M.; Fasolino, A.; Molinari, E.; Righi, M. C., Potential Energy Surface for Graphene on Graphene: Ab Initio Derivation, Analytical Description, and Microscopic Interpretation. *Physical Review B* **2012,** *86* (24), 245434.
16. Liu, Z.; Yang, J.; Grey, F.; Liu, J. Z.; Liu, Y.; Wang, Y.; Yang, Y.; Cheng, Y.; Zheng, Q., Observation of Microscale Superlubricity in Graphite. *Physical Review Letters* **2012,** *108* (20), 205503.
17. Leven, I.; Krepel, D.; Shemesh, O.; Hod, O., Robust Superlubricity in Graphene/h-BN Heterojunctions. *The Journal of Physical Chemistry Letters* **2013,** *4* (1), 115-120.
18. Hod, O., The Registry Index: A Quantitative Measure of Materials′ Interfacial Commensurability. *ChemPhysChem* **2013,** *14* (11), 2376-2391.
19. Woods, C. R.; Britnell, L.; Eckmann, A.; Ma, R. S.; Lu, J. C.; Guo, H. M.; Lin, X.; Yu, G. L.; Cao, Y.; Gorbachev, R. V.; Kretinin, A. V.; Park, J.; Ponomarenko, L. A.; Katsnelson, M. I.; Gornostyrev, Y. N.; Watanabe, K.; Taniguchi, T.; Casiraghi, C.; Gao, H. J.; Geim, A. K.; Novoselov, K. S., Commensurate–Incommensurate Transition in Graphene on Hexagonal Boron Nitride. *Nature Physics* **2014,** *10* (6), 451-456.
20. van Wijk, M. M.; Schuring, A.; Katsnelson, M. I.; Fasolino, A., Moiré Patterns as a Probe of Interplanar Interactions for Graphene on *h*-BN. *Physical Review Letters* **2014,** *113* (13), 135504.